

# **1 Numerical modeling of iceberg capsizing responsible 2 for glacial earthquakes**

Amandine Sergeant<sup>1,2,3</sup>, Vladislav A. Yastrebov<sup>4</sup>, Anne Mangeney<sup>1,2,5</sup>,

Olivier Castelnaud<sup>6</sup>, Jean-Paul Montagner<sup>1,2</sup>, Eléonore Stutzmann<sup>1</sup>

---

A. Sergeant, Versuchsanstalt für Wasserbau, Hydrologie und Glaziologie, ETH Zürich, Hönggerberggring 26, 8093 Zürich, Switzerland. (sergeant@vaw.baug.ethz.ch)

V. A. Yastrebov, MINES ParisTech, PSL Research University, Centre des Matériaux, CNRS UMR 7633, BP 87, 91003 Evry, France. (vladislav.yastrebov@mines-paristech.fr)

O. Castelnaud, Procédés et Ingénierie en Mécanique et Matériaux (UMR 8006), CNRS, ENSAM, CNAM, 151 Bd de l'Hopital, 75013 Paris (olivier.castelnaud@ensam.eu)

A. Mangeney, Institut de Physique du Globe de Paris, 1 rue Jussieu 75005, Paris, France. (mangeney@ipgp.fr)

J.-P. Montagner, Institut de Physique du Globe de Paris, 1 rue Jussieu 75005, Paris, France. (jpm@ipgp.fr)

E. Stutzmann, Institut de Physique du Globe de Paris, 1 rue Jussieu 75005, Paris, France. (stutz@ipgp.fr)

<sup>1</sup>Institut de Physique du Globe de Paris,

3 **Abstract.** The capsizing of icebergs calved from marine-terminating glaciers  
4 generate horizontal forces on the glacier front, producing long-period seis-  
5 mic signals referred to as glacial earthquakes. These forces can be estimated  
6 by broadband seismic inversion but their interpretation in terms of magni-  
7 tude and waveform variability is not straightforward. We present a numer-  
8 ical model for fluid drag that can be used to study buoyancy-driven iceberg

---

CNRS UMR 7154, Université Paris

Diderot-Paris 7, Paris, France

<sup>2</sup>Université Paris Diderot, Paris, France

<sup>3</sup>Now at Versuchsanstalt für Wasserbau,  
Hydrologie und Glaziologie (VAW), ETH  
Zürich, CH-8092 Zürich, Switzerland  
(sergeant@vaw.baug.ethz.ch)

<sup>4</sup>MINES ParisTech, PSL Research  
University, Centre des Matériaux, CNRS  
UMR 7633, Evry, France

<sup>5</sup>ANGE team, INRIA, Laboratoire  
Jacques-Louis Lions, Paris, France

<sup>6</sup>Processes and Engineering in Mechanics  
and Materials, CNRS UMR 8006, ENSAM,  
CNAM, Paris, France

9 capsize dynamics and the generated contact-forces on a calving face using  
10 the finite-element approach. We investigate the sensitivity of the force to drag  
11 effects, iceberg geometry, calving style and initial buoyancy. We show that  
12 there is no simple relationship between force amplitude and iceberg volume,  
13 and similar force magnitudes can be reached for different iceberg sizes. The  
14 force history and spectral content varies with the iceberg attributes. The ice-  
15 berg aspect ratio primarily controls the capsize dynamics, the force shape  
16 and force frequency whereas the iceberg height has a stronger impact on the  
17 force magnitude. Iceberg hydrostatic imbalance generates contact-forces with  
18 specific frequency peaks that explain the variability in glacial earthquake dom-  
19 inant frequency. For similar icebergs, top-out and bottom-out events have  
20 significantly different capsize dynamics leading to larger top-out forces es-  
21 pecially for thin icebergs. For realistic iceberg dimensions, we find contact-  
22 force magnitudes that range between  $5.6 \times 10^{11}$  kg.m and  $2 \times 10^{14}$  kg.m,  
23 consistent with seismic observations. This study provides a useful framework  
24 for interpreting glacial earthquake sources and estimating the ice mass loss  
25 from coupled analysis of seismic signals and modeling results.

## 1. Introduction

26 Rapid glacier thinning and increasing calving rates have been measured at marine-  
27 terminating glacial termini in Greenland since the 2000's [e.g. *Joughin et al.*, 2004; *Howat*  
28 *et al.*, 2007]. This rise in the number of calving events is synchronous with an increase of  
29 particular cryoseismic events referred to as glacial earthquakes [e.g. *Ekström et al.*, 2003;  
30 *Nettles and Ekström*, 2010; *Veitch and Nettles*, 2012; *Olsen and Nettles*, 2017]. Iceberg  
31 calving and, more generally, instabilities in the margins of tidewater glaciers, generate a  
32 wide spectrum of seismic signals. Signal characteristics differ due to various source mech-  
33 anisms [*Podolskiy and Walter*, for a review]. In particular, for calving events, seismic  
34 emissions can be associated with ice fracturing [e.g. *O'Neel et al.*, 2007; *Walter et al.*,  
35 2010], iceberg scraping or impacting on the calving front [*Tsai et al.*, 2008; *Amundson*  
36 *et al.*, 2008; *Walter et al.*, 2012], ice avalanches [*Sergeant et al.*, 2016], ice-mélange dy-  
37 namics [*Amundson et al.*, 2010; *Sergeant et al.*, 2016], glacier deformation, lift and basal  
38 slip [*Tsai et al.*, 2008; *Murray et al.*, 2015a], or a complex combination of these processes.  
39 All of them can occur simultaneously during a calving sequence and it is not easy to dis-  
40 tinguish between the seismic signals generated by each source mechanism [*Sergeant et al.*,  
41 2016]. The seismic source characteristics (amplitude, duration and evolution with time)  
42 are related to the dynamic processes that are involved. They should depend on rheological  
43 and dimensional parameters as has been shown for landslide events [*Favreau et al.*, 2010;  
44 *Moretti et al.*, 2012; *Ekström and Stark*, 2013; *Moretti et al.*, 2015; *Zhao et al.*, 2014;  
45 *Yamada et al.*, 2018a, b]. Detailed comparison of the force history inverted from seismic  
46 data with the force calculated by landslide models provides a unique way to determine

47 the characteristics and dynamics of natural landslides. Glacial earthquake interpretation  
48 and characterization in terms of source mechanisms and ice mass loss are therefore lim-  
49 ited since dynamic processes are difficult to quantify and discriminate between each other.

50  
51 Glacial earthquakes produce long-period waves (10-150 s) that propagate over tele-  
52 seismic distances (i.e.  $\geq 1000$  km). Generated seismic waves are best modeled with a  
53 near-horizontal source-force acting and pointing upglacier, normal to the calving front  
54 [e.g. *Veitch and Nettles*, 2012; *Walter et al.*, 2012; *Olsen and Nettles*, 2017]. Using a me-  
55 chanical model, *Tsai et al.* [2008] first showed that among all possible cryogenic sources,  
56 only basal slip and iceberg capsizing (ice-block rotation in water with contact against  
57 the glacier terminus) were able to produce high magnitude and long-period cryoseismic  
58 signals. They further showed that the contact force produced by a tipping iceberg on the  
59 calving front is the prevailing source for glacial earthquakes. However, to determine the  
60 observed range of force amplitudes and durations derived from seismic data inversions,  
61 they needed to modify the rotating iceberg inertia due to the presence of ice-mélange in  
62 the proglacial fjord.

63 *Sergeant et al.* [2016] inverted the force for a calving episode captured at the Jakobshavn  
64 Isbrae, using the broadband seismic signals at frequencies of dominant energy 0.01-0.1 Hz.  
65 In particular, they found similar durations ( $\sim 150$  s) and amplitudes ( $\sim 1 \times 10^{10}$  N) for  
66 the forces associated with the bottom-out (BO) and top-out (TO) capsizes of two icebergs  
67 of different sizes. However, the difference between the forces generated by BO (i.e. the  
68 iceberg bottom drifts away from the terminus while rotating) and TO (i.e. the iceberg top  
69 drifts away from the terminus) capsizes is not reproduced by the model proposed by *Tsai*

70 *et al.* [2008], even though such a difference is also observed in laboratory experiments of  
71 iceberg capsizes [Amundson *et al.*, 2012a]. Field and laboratory observations reveal that  
72 glacial earthquake magnitude appears to depend not only on the iceberg volume, but  
73 also on the capsize dynamics related to the calving style. Tsai *et al.* [2008] and Walter  
74 *et al.* [2012] showed that the synthetic long-period seismic waveforms are insensitive to the  
75 choice of the force time-function, notably due to filtering effects. Nevertheless, the force  
76 inverted by Sergeant *et al.* [2016] shows a complex history that varies from one event to  
77 another and cannot be described exactly by simple force-source models that have a limited  
78 number of parameters. To interpret the complexity and variability of the time-evolution  
79 of the force inverted from seismic data, a precise mechanical model for iceberg capsize is  
80 needed.

81  
82 Tsai *et al.* [2008] and then Amundson *et al.* [2012a] first derived models for the contact  
83 force between a box-shaped rigid block capsizing in water against a vertical wall. Tsai  
84 *et al.* [2008] used an added mass to model the additional inertia of the iceberg due to the  
85 water-mass displacement during its motion, and neglected energy dissipation due to water  
86 drag and viscous effects. Amundson *et al.* [2012a] accounted for the contribution of water  
87 drag to the capsize dynamics. They tested several drag force laws to compute iceberg  
88 capsize motion and generated contact forces which were then fitted to cm-scale labora-  
89 tory measurements conducted at intermediate Reynolds number  $Re \approx 10^4$ . Their analysis  
90 reveals that accounting for water drag is crucial for reproducing the observations and that  
91 most of the potential-energy excess of the capsizing iceberg is dissipated. Both model-  
92 ing approaches [Tsai *et al.*, 2008; Amundson *et al.*, 2012a] show that the contact-force

93 history depends on the iceberg dimensions, on the hydrodynamic forces (including hydro-  
94 static pressure and depending on the model: added mass or drag forces) and also on the  
95 capsize dynamics. Therefore, even for these oversimplified models of iceberg/water/wall  
96 interaction, the analytical expression of the force can hardly be derived in a closed form.

97 Here we propose an alternative model for capsizing iceberg which accounts for hydro-  
98 static pressure and approximately for dynamic fluid-structure interactions (pressure drag).  
99 This model is integrated in a finite element framework and therefore is compatible with  
100 elastic deformation of floating (and interacting) solids. The used drag model is more  
101 accurate than what was used in *Amundson et al.* [2012a], and is thus able to capture an  
102 important difference between top-out and bottom-out capsize; however, the added mass  
103 is not taken into account in our model. A detailed comparison of our model with the  
104 existing ones is provided in section 2.2.3.

105  
106 Following the work of *Tsai et al.* [2008], *Amundson et al.* [2012a] and *Burton et al.*  
107 [2012], the aim of this study is to more deeply explore the dynamic processes involved in  
108 glacial earthquakes and their influence on the generated forces. We investigate in detail  
109 the capsizing-force variation in terms of amplitude, duration, shape and spectral content  
110 with iceberg dimensions and the initial configuration. We compile catalogs of simulated  
111 force histories to guide the interpretation of forces inverted from glacial earthquakes.

112 The paper is organized as follows. We first present our model of fluid-structure interac-  
113 tion and compare it with existing models (Section 2). In Sections 3 and 4, we analyze the  
114 results for the force generated by BO and TO capsizing of icebergs of variable dimensions  
115 and compare them to other available observations (laboratory experiments and seismic

116 inversions). Finally, in Section 5, we show the influence of the initial buoyant conditions  
117 of the icebergs on the generated forces. Our conclusions emphasize the potential of our  
118 approach for the quantification of iceberg characteristics from seismic signals.

119

## 2. Iceberg-capsize model

120 We study the interaction between a box-shaped iceberg capsizing in the sea and an  
121 immobile vertical wall, which represents the post-calving front of the glacier (Figure 1).  
122 In nature, the height of capsizing icebergs that produce glacial earthquakes is observed  
123 to be the full glacier thickness as this kind of calving occurs when the glacier terminus  
124 is near-grounded [*Amundson et al.*, 2008, 2010]. The iceberg width is determined by the  
125 crevasse network and may vary over a large distance of up to tens of km. To capsize  
126 spontaneously, icebergs should have a relatively small aspect ratio (width/height  $< 0.75$ ).  
127 Since their motion is constrained by the glacier terminus, these unstable icebergs drift  
128 outward and rise up while rotating. Icebergs of greater aspect ratios are buoyantly stable  
129 and will not capsize without additional perturbations [*Burton et al.*, 2012].

130 The iceberg drift and rotational motion implies a contact interaction between the ice-  
131 berg and the glacier terminus. The evolution of the contact force, which is transmitted  
132 to the solid Earth, is controlled by the iceberg's capsize dynamics, which is primarily  
133 determined by its interaction with sea water.

134

135 The process of iceberg's capsize and the associated behavior of the glacier being complex,  
136 several simplifications are made in our model. The main assumption is the simplified fluid-  
137 structure interaction, which does not resolve costly Navier-Stokes equations including free

138 surface, friction and contact between deformable solids. It is assumed that the fluid  
139 exerts on the iceberg a depth-dependent hydrostatic pressure and resists to iceberg's  
140 motion via the pressure drag, whose detailed description is given below. Real glaciers  
141 obey an elasto-viscoplastic mechanical behavior [e.g. *Vaughan, 1995; Castelnaud et al.,*  
142 *2008; Montagnat et al., 2014*]. Here, for the sake of simplicity, the deformation of the  
143 glacier is not taken into account similarly to existing models [*Tsai et al., 2008; Amundson*  
144 *et al., 2012a*]. Crack initiation and propagation between the iceberg-to-be-calved and  
145 the terminus [e.g. *Krug and Durand, 2014*] is also neglected in our model since it can  
146 be considered that this process involves only high-frequency ( $\geq 1$  Hz) energy [e.g. *Tsai*  
147 *et al., 2008; Amundson et al., 2010*], and thus is of no interest for the low-frequency band  
148 in which glacial earthquakes are studied. The iceberg is thus assumed to be initially  
149 detached and tilted by a small angle. Finally, during the interaction of the calved iceberg  
150 with the terminus, ice fracturing and avalanches are also observed [*Amundson et al.,*  
151 *2010; Sergeant et al., 2016*] which are associated with energy dissipation and therefore can  
152 affect the overall system dynamics. These details were not taken into account neither. In  
153 addition, a recent work suggested that iceberg capsizing may induce a low-pressure zone  
154 beneath the floating tongue of the glacier [*Murray et al., 2015a*]. These authors argue  
155 that the resulting downward bending of the ungrounded terminus may be responsible for  
156 at least a part of the vertical component of the glacial earthquake force. This effect is not  
157 considered in our model and will be dealt with in future work.

## 2.1. Problem set-up

158 We investigate the capsize of an iceberg with a rectangular section of height  $H$  and  
159 width  $W$ . We define the iceberg aspect ratio as  $\epsilon = W/H$  (Figure 1). The iceberg's

160 motion is restricted by an immobile vertical wall representing the glacier's terminus. We  
 161 use a coordinate system in which the axis  $\mathbf{e}_z$  is vertical upwards, and  $\mathbf{e}_x$  is horizontal  
 162 pointing towards the glacier terminus. We denote by  $\rho_i$  the ice density (numerical values  
 163 are listed in Table 1),  $m = \rho_i HW$  is the iceberg mass, and  $G$  denotes its center of mass.  
 164 Iceberg rotation is expressed by the angle  $\theta$  measured clockwise from the vertical.

165 The iceberg is partly submerged in water (density  $\rho_w$ ). The water surface elevation  
 166 controls the hydrostatic equilibrium of the iceberg at the capsize initiation. We de-  
 167 note by  $z_w$  the water level corresponding to neutral buoyancy (i.e. iceberg at verti-  
 168 cal equilibrium if  $\theta = 0$ ). Neutral buoyancy at small initial angle  $\theta_0$  is obtained for  
 169  $z_w - z_G = H \cos \theta_0 \left( \frac{\rho_i}{\rho_w} - \frac{1}{2} \right)$  when the top of the iceberg surface lies entirely above sea  
 170 level ( $z_G$  gives the vertical position of the center of mass  $G$ ). As the glacier terminus is  
 171 not necessarily neutrally buoyant at the moment of iceberg's release, we also investigate  
 172 how the initial water level affects the capsize dynamics and the generated force. We call  
 173  $z_0$  the actual water level and  $\Delta z = z_0 - z_w$  the specified water level perturbation around  
 174 the equilibrium level.

175 An initial small iceberg tilt  $\theta_0$  is specified. We used  $\theta_0 = 1^\circ$  for bottom-out (BO)  
 176 events, and  $\theta_0 = -1^\circ$  for top-out (TO) events. The upper right or lower right corners are  
 177 in contact with the terminus at time  $t = 0$ , respectively for BO and TO events. Note  
 178 that the initial tilt angle affects the duration of the calving event, given that the iceberg  
 179 initially moves very slowly away from its unstable equilibrium position  $\theta = 0^\circ$ , but as long  
 180 as the initial angle remains small it does not affect the resulting contact-force's evolution  
 181 at later stages.

182 For sake of simplicity we assume a purely elastic behavior of the ice. Like *Petrenko and*  
 183 *Whitworth* [1999] and *Montagnat et al.* [2014], we used Young’s modulus  $E = 9.3$  GPa  
 184 and Poisson ratio  $\nu = 0.3$ . although some field measurements suggest smaller values of  
 185  $E$  [*Vaughan*, 1995]. The resulting elastic deformation occurring in the iceberg under the  
 186 action of water and contact is negligible and does not affect its dynamics and the resulting  
 187 contact force, i.e. the motion of the deformable iceberg is indistinguishable from the rigid  
 188 iceberg considered in *Tsai et al.* [2008].

189 Since we study a two-dimensional problem here, all forces  $F$  have units N/m and rep-  
 190 resent the linear force density in the  $y$ -direction (Figure 1). The real force acting on a 3D  
 191 box-shaped iceberg of a given length  $L$  along the calving front can be estimated as  $F \times L$   
 192 when  $L$  is large compared to  $H$ .

## 2.2. Iceberg dynamics

### 193 2.2.1. Formulation

The iceberg is subjected to the following forces which are time dependent (except the constant ice weight): (I) The ice weight  $\mathbf{F}_g = -\rho_i W H g \mathbf{e}_z$  ( $g$  is the gravitational acceleration). (II) The upward buoyant force  $\mathbf{F}_{hs}$  associated with the hydrostatic water pressure, which at depth  $z_0 - z$  is given by  $\rho_w g(z_0 - z)$ , and thus

$$\mathbf{F}_{hs} = -\rho_w g \int_{\Gamma^{sub}} (z_0 - z) \mathbf{n}(\mathbf{r}) d\Gamma, \tag{1}$$

194 where  $\mathbf{n}(\mathbf{r})$  is the local outward normal vector of the iceberg surface at position  $\mathbf{r}$  and  
 195  $\Gamma^{sub}$  is the contour of the submerged surface (Figure 2). (III) The frictional contact force  
 196  $\mathbf{F}_c = F_x \mathbf{e}_x + F_z \mathbf{e}_z$  acting at a corner of the iceberg. The sliding of the iceberg against  
 197 the immobile wall is assumed to be governed by Coulomb’s friction law. The vertical

198 component of the contact force,  $F_z$ , is then equal to the horizontal force component  $F_x$   
 199 multiplied by the ice-ice dynamic friction coefficient  $\mu$ :  $|F_z(t)| = \mu|F_x(t)|$  when sliding  
 200 occurs. Possible values for  $\mu$  are discussed in Appendix B. (IV) The fluid drag force  $\mathbf{F}_D$   
 201 resulting from the interaction between the moving iceberg and the surrounding water,  
 202 which opposes iceberg's motion.

The drag force depends on the fluid density, viscosity and flow regime and varies in response to the complex fluid motion around the object. Two types of drag forces can be distinguished: pressure and friction drag. Pressure drag ( $\mathbf{F}_{D_p}$ ) is equal to the integral of the fluid over-pressure along the solid (the term over-pressure is used here to highlight this pressure compared to the background hydrostatic pressure of water), and friction drag ( $\mathbf{F}_{D_f}$ ) is the integral of shearing forces appearing due to local shearing of the fluid layer in tangential motion. To determine accurately these drag forces, a direct numerical simulation of iceberg rotation in water with a free surface, governed by the Navier-Stokes equation, would be needed. However, direct solution of these equations in presence of deformable solids and contact dynamics is highly challenging. To simplify the problem, we assume that the over-pressure at every elemental area of the iceberg's surface is given by

$$\mathbf{p}_d = -\frac{C}{2}\rho_w v_n^2 \text{sign}(v_n)\mathbf{n}, \quad (2)$$

where  $\mathbf{v}$  is the iceberg velocity at the considered position  $\mathbf{r}$ ,  $v_n = \mathbf{v} \cdot \mathbf{n}$  is the normal component of this velocity, and  $C$  is a dimensionless scaling coefficient. We assume here  $C \approx 1$  as suggested by the analysis of *Munson et al.* [2012]. Note also that we assume that the relative fluid-solid velocity is determined solely by the solid velocity  $\mathbf{v}$ . The resulting

pressure-drag force (linear density) is then computed as

$$\mathbf{F}_{\mathcal{D}_p} = -\frac{\rho_w}{2} \int_{\Gamma^{sub}} v_n^2 \text{sign}(v_n) \mathbf{n} d\Gamma \quad (3)$$

203 The friction drag can be considered to be proportional to  $Re^{-1/2}$  [Munson *et al.*, 2012,  
 204 p. 489-502] where  $Re = \rho_w V L / \mu_w$  is the Reynolds number with  $V$  being the average  
 205 relative velocity of the calving iceberg with respect to the fluid,  $L$  a characteristic dimen-  
 206 sion which can be taken to be one fourth of the iceberg perimeter, i.e.  $L = H(1 + \epsilon)/2$ ,  
 207 and  $\mu_w$  the dynamic viscosity of the water. As it is discussed in Appendix A, for a  
 208 km-scale capsizing iceberg, the Reynolds number is of the order of  $10^{11}$ . Consequently,  
 209 the friction drag  $\mathbf{F}_{\mathcal{D}_f}$  can be reasonably neglected compared to the pressure drag. The  
 210 former is thus not included in the general force balance. A more detailed justification of  
 211 the choices made in our hydrodynamic model is presented in section 2.2.3 and Appendix A.

212

Neglecting the deformation of the iceberg leads to a simple system of equations for the  
 coordinates  $\mathbf{r}_G$  of the center of mass  $G$  and the inclination angle  $\theta$  (Newton's second law):

$$\begin{cases} m \ddot{\mathbf{r}}_G = \mathbf{F}_g + \mathbf{F}_{hs} + \mathbf{F}_c + \mathbf{F}_{\mathcal{D}_p} \\ I \ddot{\theta} = M_{hs} + M_c + M_{\mathcal{D}} \end{cases} \quad (4)$$

213 where  $m = \rho_i H W$  is the linear mass density,  $M_{hs}$ ,  $M_c$ , and  $M_{\mathcal{D}}$  are the moments of the cor-  
 214 responding forces  $F_{hs}$ ,  $F_c$ ,  $F_{\mathcal{D}}$  calculated at the center of mass  $G$ , and  $I = m(H^2 + W^2)/12$   
 215 is the moment of inertia computed at the center of mass. Note that we neglected the added  
 216 water mass and added hydrodynamic moment of inertia [Wendel, 1956], which were partly  
 217 taken into account in the model from Tsai *et al.* [2008].

218

## 219 2.2.2. Numerical implementation

220 Since our long-term aim is to investigate the seismic signals generated by a large variety  
221 of capsizing icebergs for various glacier/iceberg/earth/sea configurations, and to study  
222 possible destabilization of the upstream glacier flow (e.g. initiation of basal slip events),  
223 the proposed simplified fluid-structure interaction model was implemented within a Fi-  
224 nite Element framework. In the future, this implementation could be readily used for  
225 this general purpose, even though for the current study a simpler rigid model would be  
226 sufficient.

227 In order to include the interaction with water (Equations 1-2), specific surface elements  
228 were implemented in Z-set finite element software [*Besson and Foerch, 1997*]. These  
229 elements incorporate the virtual work of the hydrostatic and drag fluid pressure into  
230 the global finite element weak formulation. Integration of drag pressures over partly  
231 submerged elements (elements which are cut by the water surface) is done only on the  
232 submerged part, which ensures discretization-independent results. Thus, since we are not  
233 interested in resulting stress fields inside the ice, the results are practically independent  
234 of the mesh density. Using a relatively long time step of 1 s (i.e. comparable to the time  
235 needed for elastic waves to travel a distance similar to the iceberg dimension) smooths  
236 the resulting force by removing high-frequency oscillations coming from wave dynamics in  
237 the presence of contact. Thanks to this time smoothing, the resulting contact force and  
238 overall iceberg dynamics is directly comparable with the dynamics of rigid models [*Tsai*  
239 *et al., 2008; Amundson et al., 2012a*]. The contact between the iceberg and the terminus  
240 wall is modeled using a node-to-segment approach within the direct method suggested  
241 in *FrancaVilla and Zienkiewicz [1975]* and *Jean [1995]*. The Hilber-Hughes-Taylor (HHT)

242 method [Hilber *et al.*, 1977] was used to integrate solid mechanics equations in time.

243

### 244 **2.2.3. Comparison to existing capsize models**

245 To model iceberg capsize, *Tsai et al.* [2008] and *Amundson et al.* [2012a] solved the mo-  
246 tion equations for a system similar to the one studied here (a rectangular iceberg against a  
247 vertical wall). As long the iceberg remains in contact with the wall, the authors calculated  
248 the horizontal and vertical positions of the iceberg center of mass, the inclination angle  
249  $\theta$ , and the horizontal contact force assuming a frictionless contact between the iceberg  
250 and the wall. The main difficulty is to model hydrodynamic effects without solving the  
251 complete set of Navier-Stokes equations for the fluid with a free surface and with a moving  
252 solid. These effects are described in different ways in *Tsai et al.* [2008] and *Amundson*  
253 *et al.* [2012a]. We propose here a new formulation for the reasons explained below.

254

255 No drag was used in *Tsai et al.* [2008], however the authors used added mass to account  
256 for the mass of displaced surrounding water [Brennen, 1982; Yvin *et al.*, 2018]. The  
257 added mass concept consists in adding to the iceberg the mass and moment of inertia  
258 of the surrounding water volume that is deflected during iceberg motion. In the motion  
259 equations (equation 4), the resulting effective iceberg mass is then the sum of the ice  
260 mass  $M_g$  and the added mass corresponding to the mass of the displaced water, which  
261 varies with the direction of iceberg motion (and similarly for the moment of inertia). In  
262 presence of the free surface, the added mass of a floating object should vary depending  
263 also on the current configuration [Brennen, 1982]. For simple geometries, the added mass

264 can be calculated analytically, when a potential fluid flow (irrotational velocity field) is  
265 considered [*Wendel, 1956*].

266 In their model, *Tsai et al.* [2008] neglected the vertical added mass, considering only a  
267 horizontal added mass depending on the iceberg dimensions and inclination  $\theta$ , and reason-  
268 ably took a constant added moment of inertia that depended on the iceberg dimensions.  
269 Undoubtly, the added mass improves the model and affects the capsize dynamics, however,  
270 solely it is not sufficient to capture it correctly nor to reproduce the difference between  
271 BO and TO events, which remain indistinguishable in that model. In our finite element  
272 model, it is possible to add a varying added mass independently in  $x$  and  $z$  directions, but  
273 since we deal only with the displacement degrees of freedom, it is impossible to introduce  
274 independently the added moment of inertia. Therefore, to preserve the consistency of the  
275 model and to keep it as simple as possible, we decided not to take added mass into account.

276  
277 *Amundson et al.* [2012a] did not take into account the added mass neither, however they  
278 accounted for the drag force and torque. The authors approximated the hydrodynamic  
279 drag by forces and a torque applied to the iceberg center of mass and proportional to the  
280 corresponding squared linear and angular velocities weighted with drag coefficients, which  
281 are assumed to be constant over time. The components of the drag force depend only on  
282 the velocity of the center of mass  $\dot{x}_G$  and  $\dot{z}_G$ , and the drag torque depends only on the  
283 rotation rate  $\dot{\theta}$ . Along each direction, the authors introduce a constant damping factor,  
284 which is estimated by fitting the model to laboratory experiments of capsizing cm-scale  
285 plastic blocks. However, since laboratory experiments involve much smaller Reynolds  
286 numbers than km-size icebergs, we believe that the direct upscaling of lab results to field

287 dimensions can be not straightforward. Moreover, as drag coefficients may vary with ice-  
288 berg dimensions and shape, application to various iceberg morphologies requires an extra  
289 calibration step which would require additional experimental studies. More importantly,  
290 the horizontal drag force does not depend on the vertical velocity nor on the inclination  $\theta$   
291 the difference between BO and TO events, like the model proposed by *Tsai et al.* [2008].  
292 The difference in iceberg characteristics and calving style could be only captured if using  
293 different sets of empirical drag coefficients for the two types of events.

294

295 The model proposed in our study differs from the existing models by a potentially more  
296 accurate drag forces, which result from locally determined drag pressures computed over  
297 submerged parts. The main advantage is that since our model is incorporated in the  
298 finite element framework, it can be used for floating and interacting deformable solids.  
299 The advantage of the locally defined drag pressure is that the resulting drag force and  
300 moment depend not only on the velocity of the center of mass and iceberg rotation rate,  
301 the local velocity of the submerged surfaces. Thus it naturally depends on the current  
302 iceberg position and tilt with respect to the free water surface. Such a coupling results in  
303 different drag effects for TO and BO events. Therefore, our model is able to reproduce  
304 the experimentally observed difference between BO and TO events even without intro-  
305 ducing an ice-mélange effect as in *Tsai et al.* [2008]. Indeed, as illustrated in Figure 3,  
306 hydrodynamic effects make BO and TO events asymmetrical. This can be easily under-  
307 stood for icebergs with small aspect ratios [*MacAyeal et al.*, 2003; *Burton et al.*, 2012;  
308 *Amundson et al.*, 2012a]. To minimize the dissipation due to the pressure drag, an ini-  
309 tially TO-oriented iceberg, while it rises, tends to flow away from the terminus following

310 a trajectory with minimal water resistance. On the other hand, for BO-oriented icebergs,  
311 the “minimal-resistance” trajectory will push the iceberg toward the calving front as it  
312 rises, thus forcing the iceberg to remain in contact with the front. Therefore, BO events  
313 last longer than TO events. This difference is not captured by the models of *Tsai et al.*  
314 [2008] and *Amundson et al.* [2012a] essentially because either the lack of the drag force  
315 or the lack of coupling of, horizontal motion, inclination angle, and drag forces in its  
316 evaluation, respectively.

317  
318 It is worth highlighting that our model for fluid-structure interaction remains approx-  
319 imative (as well as other aforementioned models) and cannot be considered as ultimate  
320 capsize model. Nevertheless, we believe that it is accurate enough and in some aspects  
321 more accurate than those which were used before for the analysis of iceberg capsize. Ob-  
322 taining a more accurate iceberg dynamics, would require solving Navier-Stokes equations  
323 in presence of a free surface and contacting solids, which is a topic at the forefront of  
324 Computational Fluid Dynamic research, and thus beyond the present study. The simple  
325 model proposed here permits to carry out a parametric study and generate an accurate  
326 enough catalog of forces produced by iceberg capsize, which is one of the objectives of the  
327 current study.

### 3. Capsize dynamics and generated forces

328 Below, we present results obtained for bottom-out (BO) and top-out (TO) capsize  
329 simulations for different aspect ratios, sizes and initial vertical positions of icebergs. A  
330 summary of possible force and duration ranges is presented in Table 2. We discuss the  
331 relation between capsize dynamics and the contact-force generated on the glacier terminus

332 and we compare the calculated force magnitudes with the ones inverted from glacial  
 333 earthquake events.

### 3.1. Iceberg motion and energy

334 Figure 4 shows the time-series of the iceberg position  $\theta(t)$ ,  $x_G(t)$  and  $z_G(t)$ , the ice-  
 335 berg potential energy  $E_{\text{pot}}$  and kinetic energy  $E_{\text{kin}}$ , and the horizontal contact force  $F_c(t)$ .  
 336 Results are presented for BO (left) and TO (right) capsizes of an iceberg with aspect  
 337 ratio  $\epsilon = 0.2$  and height  $H = 800$  m and which is initially neutrally buoyant ( $\Delta z = 0$ ).  
 338 Corresponding illustrative movies are available in the supplementary material (Movies  
 339 S1 and S2). Capsize dynamics is different for different calving styles. For both BO and  
 340 TO capsizes, the maximum kinetic energy is significantly lower (more than one order of  
 341 magnitude) than the total gravitational potential energy that is released. The ratio of  
 342 maximum kinetic energies BO/TO is  $\sim 0.4$  which is in good agreement with the measure-  
 343 ments of *Amundson et al.* [2012a] for plastic blocks of aspect ratio  $\epsilon = 0.25$ . Note that  $E_{\text{kin}}$   
 344 is the same for BO and TO rotations if the drag is not accounted for (black dashed lines  
 345 in Figure 4b). In contrast, the  $E_{\text{kin}}$  calculated with the drag is about 6 times smaller than  
 346 that calculated without drag for BO capsizes, and about 3 times smaller for TO capsizes.  
 347 This shows that pressure drag has a stronger effect on BO than on TO iceberg capsizes  
 348 style. The differences between BO and TO capsizes come from the presence of the wall  
 349 and related hydrodynamics, as detailed in section 2.2.3. This supports the observations  
 350 made by *Burton et al.* [2012] and *Amundson et al.* [2012a] of energy dissipation measured  
 351 in laboratory experiments for BO and TO events.

352

### 3.2. Force history

353 From the onset of capsize, the contact force (black lines in Figure 4c) increases, reaching  
354 a maximum for angle  $\theta_M$ , and then decreases with a higher rate until loss of contact at  
355  $\theta_C$ . This results in smoothed-triangle like shaped horizontal force with dominant spectral  
356 content below 0.1 Hz. The red lines in Figure 4c represent forces after bandpass filtering  
357 in the glacial earthquake frequency band. We used a zero-phase Butterworth filter with  
358 corner frequencies 0.01 and 0.1 Hz. Filtered forces exhibit changes of their amplitude  
359 polarity at approximately the time of the loss of contact, called the centroid time and  
360 denoted by  $t_c$ . The waveform of the filtered force can then be roughly approximated by a  
361 Centroid Single Force model (CSF, thick red line in Figure 4c) which is the source model  
362 commonly used in glacial earthquake seismic wave modeling [*Tsai and Ekström, 2007*;  
363 *Tsai et al., 2008*; *Veitch and Nettles, 2012*]. For both BO and TO capsizes, 0.01-0.1 Hz  
364 filtered forces have lower amplitudes than the actual forces (by a factor larger than 2  
365 here). This factor obviously depends on the frequency band of the filter and also on  
366 the frequency content of  $F_c$  that varies with calving style, iceberg dimensions and initial  
367 buoyancy conditions, as discussed later.

368 Iceberg capsize is a slow process which thus generates long-period seismic waves. Glacial  
369 earthquakes are generally observed to have dominant seismic frequency around 0.015-0.02  
370 Hz [*Tsai and Ekström, 2007*]. The depletion in high-frequency energy of glacial earth-  
371 quakes ( $> 1$  Hz) is not a seismic wave propagation effect, but is produced by the source  
372 mechanism itself [*Ekström et al., 2003*]. The lower frequency corner of the band-limitation  
373 should be related to the source duration. However, it is difficult to distinguish discrete  
374 seismic signals at frequencies below 0.01 Hz from other strong continuous noise or other

375 calving-generated phenomena [*Amundson et al.*, 2012b; *Walter et al.*, 2013; *Sergeant et al.*,  
 376 2016]. That is why we will refer to filtered forces between 0.01 Hz and 0.1 Hz for inter-  
 377 preting glacial earthquakes.

378  
 379 The simulated TO and BO forces are different. The TO capsize is more rapid than  
 380 the BO capsize presented here resulting in a shorter TO force duration  $T$  ( $T^{TO} = 115$  s  
 381 and  $T^{BO} = 145$  s). The TO force reaches its maximum at  $\theta_M \approx 30^\circ$  and is released  
 382 when  $\theta_C \approx 48^\circ$ . For the BO case,  $\theta_M \approx 32^\circ$  and  $\theta_C \approx 70^\circ$ . This results in a TO force  
 383 that increases more rapidly to its maximum value than the BO force and then decreases  
 384 more abruptly to zero. As a result, capsize of a given iceberg will produce different  
 385 seismic signals depending on whether it capsizes in BO or TO style. As discussed above  
 386 and concluded in the experiments of *Amundson et al.* [2012a], the difference between the  
 387 forces generated by these two capsize styles comes from hydrodynamic effects. Indeed,  
 388 when no pressure drag is accounted for (dashed lines in Figure 4c), BO and TO horizontal  
 389 forces are identical.

### 3.3. Impact of hydrodynamics on force magnitude and comparison with seismic inversion

For the sake of consistency with previous studies [*Tsai et al.*, 2008; *Veitch and Nettles*, 2012], we compute the so-called magnitude  $A$  by integrating the force history  $F_c(t)$  twice:

$$A = \int_0^{T'} \int_0^t F_c(t') dt' dt. \quad (5)$$

390 The quantity  $A$  has units of kg.m and can represent a product mass  $\times$  displacement for the  
 391 iceberg or the calving glacier. Results are presented for iceberg aspect ratios  $0.1 \leq \epsilon \leq 0.7$ ,  
 392 heights  $500 \text{ m} \leq H \leq 1050 \text{ m}$ , and lengths  $500 \text{ m} \leq L \leq 5000 \text{ m}$ . These dimensions corre-

393 spond to icebergs that can capsize spontaneously and that have the full glacier thickness  
 394 [e.g. *Bamber et al.*, 2001; *Amundson et al.*, 2008] and an across-glacier length that does  
 395 not exceed average glacier width in Greenland.

396  
 397 Figure 5 shows simulated magnitude  $A$  as a function of the effective force duration  $T'$   
 398 for BO (black crosses) and TO (green crosses) capsizes when  $L = 5000$  m. Note that  
 399 the duration of the force generated during the entire capsize process ( $T_{\theta_0-\theta_c}$ ) strongly  
 400 depends on the iceberg initial tilt  $\theta_0$ : the smaller  $\theta_0$  is, the longer it takes to initiate the  
 401 capsize, resulting in a smoother increase of the force. To get rid of this  $\theta_0$ -dependency,  
 402 here we define  $T'$  values as the duration for which the force rate  $\dot{F}_c(t)$  is above the 20%  
 403 threshold of the maximal force rate:  $|\dot{F}_c| \leq 0.2 \max(|\dot{F}_c|)$ . Orange and red lines represent  
 404 the evolution of  $A(T')$  for TO and BO icebergs with  $\epsilon = 0.5$  and  $L = 5000$  m, respectively.  
 405 We find significantly different results from those obtained with the model of *Tsai et al.*  
 406 [2008] (dashed pink line, see also their Figure 7) in which no drag was used. Comparisons  
 407 between our modeling results and those of *Tsai et al.* [2008] demonstrate the importance  
 408 of water drag for capturing and discriminating BO and TO capsize dynamics. Accounting  
 409 for drag forces results in higher magnitudes  $A$  compared to those computed without drag  
 410 (Figures 4 and S1), especially for thin icebergs. These results are in good agreement with  
 411 the observations of [*Amundson et al.*, 2012a, Figure 5b].

412  
 413 Finally, to interpret glacial earthquakes, we have to investigate the capsize response in  
 414 the seismic band. For direct comparison to the source parameters inverted from seismic  
 415 records, we compute the CSF magnitudes  $A_{CSF}$  by integrating twice the CSF models that

416 best-fit the 0.01-0.1 Hz filtered force histories. Blue dots in Figure 5 indicate lower and  
 417 upper boundaries for  $A_{CSF}$  values calculated from our simulations with varying  $L$ . We  
 418 find  $A_{CSF}$  values that range between  $5.6 \times 10^{11}$  and  $2 \times 10^{14}$  kg.m. From the inversion of  
 419 300 events in Greenland, *Tsai and Ekström* [2007] and *Veitch and Nettles* [2012] find a  
 420 range of  $A_{CSF}$  between  $2 \times 10^{13}$  kg.m and  $2.1 \times 10^{14}$  kg.m (blue box in Figure 5), the lower  
 421 bound being associated with detection limits. Our modeling results are therefore in very  
 422 good agreement with seismic observations. Without introducing an ice-mélange effect,  
 423 they indicate that icebergs capsizing against the calving front generate a force compatible  
 424 with glacial earthquake generation.

#### 4. Force variations with iceberg dimensions ( $\epsilon$ , $H$ )

425 We investigate now the sensitivity of the force (duration, maximum amplitude, magni-  
 426 tude, force history) to iceberg dimensions (aspect ratio  $\epsilon$  and height  $H$ ) during BO and  
 427 TO capsize events.

##### 4.1. Bottom-out capsize

428 Figure 6 shows the (a) actual duration  $T$  and (b) maximum amplitude of the force  
 429 as a function of  $\epsilon$  and  $H$ . Here  $T$  is the actual duration of the force (equal to  $T_{\theta_0-\theta_c}$ )  
 430 in contrast to  $T'$  which was introduced before to describe the effective duration of the  
 431 significant force to be compared with results of *Tsai et al.* [2008].  $T$  ranges between 100  
 432 and 300 s meaning that the BO capsize process (from  $\theta = 1^\circ-90^\circ$ ) can last in the field  
 433 up to 6 min as reported in [*Amundson et al.*, 2008; *Walter et al.*, 2012].

434 For a fixed aspect ratio, both force duration and amplitude increase with iceberg height.  
 435 By best fitting the results for a given  $\epsilon$ , we find that  $T$  roughly scales as  $H^\alpha$  with  $\alpha$  varying

436 between 0.65 and 0.75 for different aspect ratios. The force duration and maximum  
 437 amplitude distributions look approximately symmetric around a given  $\epsilon_0$ . For every height  
 438  $H$ ,  $T$  is minimum at  $\epsilon_0 \approx 0.35$ . Similarly, the contact force is maximum at  $\epsilon_0 \approx 0.4$ . The  
 439 latter observation is in good agreement with analytical solutions proposed by *MacAyeal*  
 440 *et al.* [2003]; *Amundson et al.* [2010]; *Burton et al.* [2012]. This means that the same force  
 441 amplitude can be reached for two capsizing icebergs of same height and different  $\epsilon \approx 0.4 \pm$   
 442  $\Delta\epsilon$ , where  $0 < \Delta\epsilon \leq 0.3$ . We find that the relative variations of the force amplitude with  
 443 iceberg dimensions can be approximately fitted with the function  $H^{2.6}\epsilon(\sqrt{1-\epsilon^2}-\epsilon)$  (black  
 444 contour lines in Figure 6b), except when  $\epsilon$  is close to its critical value for spontaneous  
 445 iceberg capsize ( $\epsilon \simeq 0.75$ ).

446 Figure 6c shows the distribution of the force magnitude  $A$  with iceberg dimensions. One  
 447 obtains that  $A$  is weakly sensitive to the aspect ratio but essentially depends on  $H$ . As a  
 448 consequence, the estimate of the iceberg volume from the contact force magnitude would  
 449 then lead to significant uncertainties. Also shown on figure 6c (black dashed contour lines)  
 450 is the analytical function  $A \sim H^3\epsilon(\sqrt{1+\epsilon^2}-\epsilon)$  obtained by *Amundson et al.* [2012a] and  
 451 *Tsai et al.* [2008] when no hydrodynamic effects are accounted for. This latter behavior,  
 452 recovered by our modelling if drag is not considered, significantly departs from results  
 453 with drag. This highlights large effect of drag forces and their parametrization.

454 When filtered in the seismic band (Figure 6d), the dependency of the maximum force  
 455 amplitude on  $(\epsilon, H)$  looks similar to that of the non-filtered case even though it is no  
 456 longer really symmetric with respect to  $\epsilon \simeq 0.4$ , especially when  $H \geq 700$  m. This analysis  
 457 clearly shows the tradeoff between  $\epsilon$  and  $H$ , i.e. several pairs  $(\epsilon, H)$  can lead to the same  
 458 force duration, amplitude or magnitude. It confirms the results of *Tsai et al.* [2008] and

459 *Amundson et al.* [2012a] that the force magnitude (or amplitude) determined from seismic  
460 data cannot be used alone to discriminate and determine the iceberg size. To illustrate  
461 this, we have plotted lines of iso-volume  $\epsilon H^2 L$ , with  $L$  kept constant (purple contour lines  
462 in Figures 6d). For the same iceberg volume, the maximum force can vary up to 80%,  
463 depending on the combination of parameters  $\epsilon$  and  $H$ .

464  
465 To further provide a quantitative validation of the model, we compare computed 0.01-  
466 0.1 Hz force amplitudes and magnitudes  $A_{CSF}$  based on best-fitting CSF models to the  
467 values inverted for two glacial earthquakes (point A and B in Figure 6d) by *Veitch and*  
468 *Nettles* [2012] using the inversion method of *Sergeant et al.* [2016]. Event A was gener-  
469 ated by an iceberg with  $L \approx 2500$  m,  $H \approx 1000$  m and  $\epsilon \approx 0.3$  (volume  $0.75 \text{ km}^3$ ) which  
470 calved BO from the Jakobshavn Isbrae glacier on 21 May 2010 [*Rosenau et al.*, 2013].  
471 It produced a force of maximum amplitude  $5.4 \times 10^{10}$  N in the radial direction, normal  
472 to the terminus that is well reproduced by our model (computed maximum amplitude of  
473  $5.9 \times 10^{10}$  N). Event B is due to the BO capsizing of an iceberg with  $L \approx 2500$  m,  $H \approx 800$  m  
474 and  $\epsilon \approx 0.23$  (volume  $0.37 \text{ km}^3$ ) from Helheim glacier, on 25 July 2013 [*Murray et al.*,  
475 2015a]. It produced a force amplitude of  $3 \times 10^{10}$  N also very well reproduced by the  
476 proposed approach (amplitude of  $2.95 \times 10^{10}$  N).

477  
478 Let us now look in more details at the change in the force history (i.e. force shape) and  
479 associated spectral amplitudes, for iceberg aspect ratios  $\epsilon = 0.1, 0.3$  and  $0.6$  and three  
480 different heights  $H = 600$  m,  $800$  m and  $1000$  m (Figure 7). For a given aspect ratio, the  
481 amplitude and duration of the force increases with  $H$  but the shape of the force is similar

482 for all  $H$ . On the contrary, when  $\epsilon$  increases, the shape of the force changes with a sharper  
 483 drop to zero when the iceberg loses contact with the terminus. The force shape is thus  
 484 essentially controlled by  $\epsilon$  as observed in laboratory experiments [*Mac Cathles et al.*, 2015].  
 485 More specifically, the capsize of thin icebergs ( $\epsilon < 0.2$ ) exerts a long duration force on the  
 486 terminus that slowly increases until its maximum at the rotation angle  $\theta_M \approx 40^\circ$  and then  
 487 smoothly decreases until the loss of contact at  $\theta_C \approx 80^\circ$ . For  $\epsilon \geq 0.2$ , force maxima are  
 488 achieved for  $\theta_M \approx 30^\circ$  and the iceberg-to-terminus contact is lost at  $\theta_C$  values decreasing  
 489 from  $70^\circ$  to  $40^\circ$  as the aspect ratio increases.

490 The variability of the force history with  $\epsilon$  then results in various spectra (Figure 7b).  
 491 For  $\epsilon < 0.2$ , the spectral amplitudes decrease more rapidly with increasing frequency than  
 492 when  $\epsilon \geq 0.2$ . This leads to much higher spectral ratios between low and high frequency  
 493 components (LF/HF ratio) for thin icebergs. An important result of this analysis is that  
 494 the change of the force shape with  $\epsilon$  can be measured in the seismic frequency band (red  
 495 lines).

## 4.2. Top-out capsize

496 The same analysis was carried out for TO events (Figure 8). As discussed in sec-  
 497 tion 3, TO and BO capsizes yield identical forces when pressure drag is not accounted for.  
 498 However, when the drag is accurately taken into account, the two forces differ since the  
 499 calving front impedes the free rotation of the iceberg. The difference manifests in shorter  
 500 TO capsize durations (up to 1.5 min) and therefore shorter TO force durations ( $100 \text{ s}$   
 501  $\leq T \leq 250 \text{ s}$ , Figure 8a first row).

502 The relative differences of the force maximum amplitude between TO and BO capsizes  
 503 show that TO force amplitudes are always higher than those of BO, except for large

icebergs with aspect ratios  $\epsilon \geq 0.6$  (Figure 8b second row). This is especially true for  
 $\epsilon < 0.2$ ,  $F_c^{TO} \geq 1.2F_c^{BO}$  (i. e. an increase of 20% in the TO case). These large differences  
arise from hydrodynamic effects that are stronger for thinner icebergs (Figure S1). In  
the seismic band 0.01-0.1 Hz, the difference in the force maximum amplitudes is even  
higher, up to 150% (Figure 8b fourth row). For example,  $F_c^{TO} \geq 1.2F_c^{BO}$  at  $\epsilon \sim 0.4$ ,  
and  $F_c^{TO} \geq 1.8F_c^{BO}$  at  $\epsilon \sim 0.2$ . . These differences are consistent with the observations  
of *Sergeant et al.* [2016] who determined inverted forces of similar amplitudes for a BO  
iceberg that was three times larger than the subsequent TO capsized iceberg along the  
same glacier terminus.

The very large variability of the maximum amplitude and duration of the force between  
TO and BO events, in the 0.01-0.1 Hz band, can be understood by looking at the dif-  
ferences of the shape and frequency content of the simulated force for different values  
of  $(\epsilon, H)$ . Figure 9 shows the force histories and associated spectral amplitudes for TO  
(solid lines) and BO (dashed lines) capsizes of icebergs with aspect ratios  $\epsilon = 0.1, 0.3$   
and 0.6. For the thinnest icebergs ( $\epsilon \leq 0.2$ ), loss of iceberg contact with the wall occurs  
much earlier for TO capsizes than for BO capsizes ( $\theta_C^{TO} \approx 55^\circ$  and  $\theta_C^{BO} \approx 80^\circ$ ). The TO  
force has a higher amplitude and drops more sharply from its maximum to zero than  
the BO force. As the aspect ratio increases, TO and BO forces tend to resemble each  
other. Interestingly, for aspect ratio  $\epsilon = 0.6$ , the BO real and filtered forces are slightly  
higher than the corresponding TO forces. Note that the force shape of TO icebergs is less  
sensitive to  $\epsilon$  than the BO force shape due to hydrodynamic effects.

## 5. Force variations with iceberg initial buoyant conditions

The glacier terminus is not necessarily at its hydrostatic equilibrium, depending on the bedrock slope, water depth, and floating ice-tongue length [e.g. *Rosenau et al.*, 2013; *James et al.*, 2014; *Murray et al.*, 2015b; *Wagner et al.*, 2016]. If the iceberg that detaches from the calving front is not neutrally buoyant at the initiation of its capsizing, it will experience up- or down-lift, possibly affecting its contact with the terminus. Those scenarios may happen if (i) the iceberg's height is smaller than the full-glacier thickness, and/or (ii) at the initiation of calving, mass loss occurs, triggered and associated with serac collapses or ice-avalanching along the calving front as it is often observed [*Amundson et al.*, 2010; *Sergeant et al.*, 2016], and/or (iii) at the time of the event, the terminus in the vicinity of the calving front is not neutrally buoyant. The latter scenario (iii) may occur for several reasons. On one hand, ungrounded glacier termini show vertical oscillations in response to the ocean tidal forcing with a time lag of a few hours, particularly before calving [e.g. *De Juan et al.*, 2010]. On the other hand, fracture leading to the formation of a full-glacier thickness iceberg is a long process that can last up to two days [*Xie et al.*, 2016]. Meanwhile, the future ice-block is likely to acquire a non-zero tilt angle (up to  $\sim 5^\circ$ ) that deviates its orientation from its initial vertical position. *Murray et al.* [2015b] measured some anomalies of the Helheim terminus elevation close to the front, right before calving. The future portion of ice-to-be-calved showed a few-meter uplift before its release and bottom-out capsizing, once the basal crevasses crossed the full-glacier thickness. Both modeling and field observations indicate that the glacier terminus can be outside its hydrostatic equilibrium with a few-meter difference with respect to its neutrally buoyant elevation.

548 We therefore investigate the change in the calving force associated with initial equilib-  
 549 rium of the iceberg by varying the water level around the iceberg buoyant state that occurs  
 550 at water elevation  $z_w$  (hydrostatic equilibrium of the ice-block). The perturbation of water  
 551 level for an initial non-neutrally buoyant iceberg,  $\Delta z = z_0 - z_w$ , is varied within the range  
 552 -10 to +10 m, where  $z_0$  is the actual water level. Icebergs that experience a waterline  
 553 with  $\Delta z < 0$  and  $\Delta z > 0$  are referred to as subaerial and submarine icebergs, respectively.

554  
 555 Figure 10 shows the time evolution and associated spectral amplitudes of the rotation  
 556 angles  $\theta(t)$ , vertical positions  $z_G(t)$  and contact forces  $F_c(t)$  that are generated by the  
 557 capsizes of a neutrally buoyant iceberg (blue lines), and a subaerial (black) or submarine  
 558 (green) iceberg.

559 Figure 11 shows the force and associated spectral amplitudes for subaerial and subma-  
 560 rine capsizing icebergs ( $\epsilon = 0.1$ ,  $H = 800$  m) for different  $\Delta z$ . Gray-shaded lines show  
 561 that the higher  $|\Delta z|$  (resulting in a higher buoyancy force), the more affected the capsize  
 562 force is. Non-neutral icebergs exert a force on the terminus with higher spectral ampli-  
 563 tudes at high frequencies, with respect to the neutral force (blue lines). We denote as  $f_{\text{plus}}$   
 564 and  $f_{\text{gap}}$  the central frequency of the peaks observed in the force spectra of non-neutrally  
 565 buoyant icebergs corresponding to amplification and decrease of frequency content, re-  
 566 spectively. Interestingly, for submarine icebergs, the amount of depleted energy at  $f_{\text{gap}}$  is  
 567 very high. The spectral amplitude perturbations at  $f_{\text{plus}}$  and  $f_{\text{gap}}$  increases with  $|\Delta z|$  and  
 568 are maximum for icebergs of aspect ratios  $\epsilon \sim 0.1$  and  $\epsilon \geq 0.6$ . Indeed the dynamics of  
 569 the thinnest and widest icebergs are much more affected by initial buoyant conditions as  
 570 these ice-blocks rotate more slowly than intermediate- $\epsilon$  icebergs (section 4.1, Figure 6a).

571 Values of  $f_{\text{plus}}$  and  $f_{\text{gap}}$  vary with  $\epsilon$  and  $H$  within the range 0.012-0.03 Hz (see Text S1  
572 and Figure S2).

573

574 Note also that a pulse in the horizontal force for subaerial icebergs can be observed in  
575 Figure 11(a), after the loss of contact with the terminus. This results from an impact  
576 of the iceberg on the wall after it has fully capsized (top left corner of the rectangular  
577 ice-block, see Figure 1). This impact can affect the filtered force (inset box in the figure)  
578 depending on the passband filter corner frequencies and the delay  $\Delta T$  between the loss of  
579 contact and the subsequent iceberg-to-terminus collision. We observe such impacts only  
580 for thin subaerial icebergs with aspect ratios  $\epsilon \leq 0.12$  (at any  $\Delta z$ -value in the investigated  
581 range down to -10 m) and for submarine icebergs with  $\epsilon \leq 0.15$  and for  $\Delta z > 6$  m.  $\Delta T$   
582 ranges from 15 to 135 s after the loss of contact. This leads to a visible impact signature  
583 that is not necessarily distinguishable from the capsize force signal if the force history  
584 is low-pass filtered with a corner frequency below  $1/(2\Delta T)$ . For example, if the impact  
585 occurs 50 s after the loss of contact, the capsize and collision signals are distinguishable  
586 in the seismic band ( $\geq 0.01$  Hz). For a  $\Delta T$  of 20 s, the two sources cannot then be dis-  
587 tinguished for frequencies below 0.025 Hz. Iceberg capsize and subsequent impact would  
588 then act like a unique seismogenic source.

589

590 Finally, note that the frequency gap due to the iceberg initial floatation level is also  
591 observed in the seismic records of glacial earthquakes and in the inverted forces. Figure 12  
592 shows the results for the force histories and associated normalized spectrograms and power  
593 spectra from (a) our modeling and (b) waveform inversion of three glacial earthquakes

594 recorded at GLISN broadband seismic stations (yellow triangles in inset maps). The data  
595 forces (red lines in b) were inverted following the method of *Sergeant et al.* [2016] in the  
596 bandpass frequency band 0.01-0.1 Hz for seismic events which occurred on 2012/01/03  
597 2012 11:11:41.7 UTC in Upernavik Isstrom; 2012/04/24 4:46:21.6 UTC in Rink glacier;  
598 and 2013/03/04 11:41:29.3 UTC in Helheim glacier. Glacial earthquake origin times and  
599 locations (red stars) were provided by *Olsen and Nettles* [2017]. Force spectra data (in  
600 red) shows specific frequencies (indicated by arrows in Figure 12) for maximum spectral  
601 peak, secondary peak or spectral gaps that are well fitted with the model force spectra  
602 computed for subaerial or submarine icebergs (black lines). These features could not  
603 be reproduced when using initially neutrally buoyant icebergs (blue lines). As spectral  
604 gaps are observed at every Greenland station that has recorded the earthquakes, our  
605 study suggests that they are a real source effect for icebergs that calve from non-neutrally  
606 buoyant terminus fronts.

## 6. Concluding remarks

607 This study presents a 2D numerical model designed to investigate BO and TO iceberg  
608 capsize dynamics and the horizontal component of the force applied on the glacier termi-  
609 nus. The model accounts for iceberg-water interactions, ice rheology and frictional con-  
610 tacts. One difficulty of this modeling approach was to design an appropriate drag model to  
611 study large scale capsize phenomena, and in particular to capture the differences between  
612 BO and TO events. Though the present model for fluid-structure interaction remains  
613 approximative and cannot be considered as ultimate capsize model it permits to carry  
614 out a parametric study and generate an accurate enough catalog of forces produced by  
615 iceberg capsize.

616 We analyzed the variations of the force shape, amplitude and duration and the spec-  
 617 tral energy distribution with iceberg dimensions (aspect ratio  $\epsilon$  and height  $H$ ), the initial  
 618 buoyant conditions and calving style. We considered the actual iceberg-to-terminus con-  
 619 tact force, but also the horizontal force component bandpass filtered in the seismic band  
 620 0.01-0.1 Hz. This study provides catalogs for the horizontal force generated by the capsize  
 621 of icebergs responsible for glacial earthquakes. Main results are:

622 1. For a fixed aspect ratio, the force duration  $T$ , amplitude and therefore magnitude  $A$   
 623 increase with iceberg height  $H$ .

624 2. For a given height, similar force amplitudes are found for aspect ratios  $\epsilon \approx 0.4 \pm \Delta\epsilon$   
 625 with  $\Delta\epsilon$  a perturbation of  $\epsilon$ .

626 3. The force time evolution (force shape) and its spectral energy distribution spectrum  
 627 modulus differs with the initial state of equilibrium of the iceberg, the calving style and  
 628  $\epsilon$ , especially for BO capsizes.

629 4. Force amplitudes and magnitudes related to BO and TO capsizes differ for icebergs  
 630 of the same dimensions. Except for very wide icebergs ( $\epsilon \geq 0.6$ ), TO icebergs exert an up  
 631 to 20% larger force on the terminus than BO capsizes and, especially in the seismic band,  
 632 TO force amplitude can be 1.5 larger than the BO 0.01-0.1 Hz filtered force. Conversely,  
 633 wide TO icebergs ( $\epsilon \geq 0.6$ ) exert a weaker force on the terminus.

634 5. For thin icebergs ( $\epsilon \leq 0.12$ ), impact against the glacier terminus occurring at  $\Delta T$   
 635 around 15 to 135 s after the loss of contact are observed in the simulation. In the studied  
 636 case, the force exerted by this impact is of the same order of magnitude of the capsize  
 637 force, and cannot necessarily be distinguished from the capsize force signal if the force  
 638 history is low-pass filtered with a corner frequency below  $1/(2\Delta T)$ .

639 A key point, in line with former studies [*Tsai et al.*, 2008; *Amundson et al.*, 2012a],  
640 is that the contact force amplitude is not uniquely defined by the iceberg volume but  
641 depends on a combination of parameters  $\epsilon$  and  $H$ ,  $\Delta z$  and also on the calving style.  
642 This implies that glacial earthquake magnitude cannot be interpreted in terms of iceberg  
643 volume only, in order to characterize ice mass loss at individual glaciers. However, an  
644 important result is that the force history carries the signature of the iceberg geometry  
645 ( $H$ ,  $\epsilon$ ), its initial buoyancy state  $\Delta z$  and its calving style. In particular, great differences  
646 in the force histories and spectra are obtained for varying distances  $\Delta z$  to the initial  
647 ice-block flotation level. The variability of the force spectral content shown in Figure 12  
648 is qualitatively observed in the forces inverted from glacial earthquake when considering  
649 icebergs out of their hydrostatic equilibrium ( $\Delta z \neq 0$ ).

650 An important point is that each of the parameters ( $\epsilon$ ,  $H$ ,  $\Delta z$ ) acts very differently on  
651 this force history. As a result, comparing the full force history inverted from seismic data  
652 to the catalog of forces calculated with our model may provide a way to determine the ice-  
653 berg characteristics (ice mass loss) from the seismic signal as done for landslides. Indeed,  
654 for landslides, combining seismic inversion and numerical modeling makes it possible to  
655 determine the characteristics of the released mass and the friction coefficient and to quan-  
656 tify physical processes acting during the flow (e. g. erosion) [*Moretti et al.*, 2012, 2015;  
657 *Yamada et al.*, 2018a, b]. To reduce the number of possible ( $\epsilon$ ,  $H$ ) combinations, one  
658 could possibly often assume that the iceberg heights are close to the glacier thickness in  
659 the margin of the calving front.

660 Finally, we derived force magnitudes that are consistent with seismic observations (Ta-  
661 ble 2). This contrasts with the results of *Tsai et al.* [2008] who obtained only order-

662 of-magnitude agreement with glacial earthquake magnitudes for calving models without  
663 ice-mélange. The presence of ice-mélange may also influence calving style and its effect on  
664 capsize dynamics and generated forces [*Tsai et al.*, 2008; *Amundson et al.*, 2010] should  
665 therefore be investigated in future work.

666

667 In addition, several features that may have consequences on glacial earthquakes have  
668 not yet been addressed, such as iceberg geometry (all studies so far have used box-shaped  
669 icebergs), complex hydrodynamics (turbulent flow, generated ocean waves), desintegration  
670 and collapse of icebergs while calving, the effect of ice-mélange, and terminus conditions  
671 and their implications for the glacier stability. At this stage, the model is limited to a  
672 configuration involving a fixed wall that does not have any floating part. For this reason,  
673 we did not compute the vertical force resulting from glacial earthquakes, which has so  
674 far been attributed to co-seismic glacier bending [*Murray et al.*, 2015a]. Investigating  
675 the vertical force component generated during the process of iceberg capsizing against  
676 an ungrounded terminus should help in the characterization of glacier ice-ice friction, the  
677 discrimination of BO from TO events and the refinement of our understanding of the  
678 cause of glacial earthquakes.

679 **Acknowledgments.** We gratefully acknowledge François Charru (IMFT) and Pauline  
680 Bonnet (IPGP) for enlightening discussions. The authors thank Olga Sergienko, Ja-  
681 son Amundson, Victor Tsai and Brad Lipovsky for their review which significantly  
682 helped to improve the manuscript. The numerical modeling was done using Z-set  
683 ([www.zset-software.com](http://www.zset-software.com)), a non-linear finite-element suite developed by the Centre des  
684 Matériaux, Mines ParisTech and Onera (France). This work has been partially funded

685 by ANR contract ANR-11-BS01-0016 LANDQUAKES, CNCS-UEFISCDI project PN-II-  
686 ID-PCE-2011-3-0045, Institut Universitaire de France and ERC contract ERC-CG-2013-  
687 PE10-617472 SLIDEQUAKES. The research was supported by a DGA-MRIS scholarship.  
688 This is IPGP contribution number XXX.

## Appendix A: Justification of the drag model

689 The proposed drag model is phenomenological, as it is based on the assumption that  
690 pressure drag scales as squared velocity of the moving solid, as in *Amundson et al.* [2012a],  
691 but is integrated locally. This remains of course a big assumption but in our case, the  
692 drag is only needed to be able to simulate the damping of the solid in fluid. To justify  
693 the choice for the used local fluid effect model, we discuss below the dependency of the  
694 friction drag on the Reynolds number and we compare pressure drag computations based  
695 on equation (3) with experimental data on a simple case study.

696  
697 The effective drag force  $F_{\mathcal{D}} = F_{\mathcal{D}_p} + F_{\mathcal{D}_f}$  and associated moment  $M_{\mathcal{D}}$  exerted on the  
698 iceberg are estimated by integrating the pressure and friction drags over the submerged  
699 surface. Experimental measurements of water drag exerted on a cylinder moving at vari-  
700 able speed show that the friction drag to total drag ratio  $F_{\mathcal{D}_f}/F_{\mathcal{D}}$  is small and decreases  
701 with the Reynolds number:  $F_{\mathcal{D}_f}/F_{\mathcal{D}}$  is 0.138, 0.0483, and 0.0158 for  $Re = 10^3$ ,  $10^4$ , and  
702  $10^5$ , respectively [*Munson et al.*, 2012, p. 516]. For a km-scale capsizing iceberg, the  
703 Reynolds number is of the order of  $10^{11}$  and therefore the drag exerted on the ice-block  
704 may be essentially due to pressure drag. This observation is also supported by the trajec-  
705 tory of icebergs in the open ocean: the drift at slow velocities of km-size icebergs in sea  
706 currents ( $Re \approx 10^9$ ) is well modeled when a very small amount of friction drag is included

707 [*Smith and Banke, 1983*]. Thus we model here iceberg capsize dynamics with the pressure  
 708 drag only.

709

710 To justify the choice of the local drag pressure, we compare pressure drag compu-  
 711 tations based on equation (3) with experimental data. We compute drag coefficients  
 712  $C_D = \frac{F_D}{0.5\rho_w V^2 A}$  for ellipsoidal bodies with different aspect ratios  $b/a$ , where  $V$  is the body  
 713 velocity relative to the fluid and  $A = La$  the area of a vertical cross section passing  
 714 through the center of the ellipse. The computed values of  $C_D$  are compared to experi-  
 715 mental measurements extracted from *Munson et al. [2012]* at  $Re = 10^5$  (Figure A1). The  
 716 model well captures the qualitative evolution of the drag coefficient and provides relatively  
 717 accurate quantitative results at small aspect ratios  $\epsilon \leq 0.7$ , which are the aspect ratios of  
 718 interest for the rectangular icebergs considered in this study. For larger aspect ratios, the  
 719 discrepancy is larger but the hydrodynamics around smooth solids elongated along the  
 720 flow direction can be considered irrelevant to flows near the capsizing icebergs.

721

722 Note that, as friction drag is not taken into account in the proposed framework, the  
 723 laboratory-scale experiments of *Amundson et al. [2012a]* cannot be reproduced with our  
 724 model as these experiments involved much smaller Reynolds numbers than those of km-  
 725 size capsizing icebergs. Capsize dynamics are probably affected by a non-negligible portion  
 726 of viscous drag.

727

## Appendix B: Sensitivity of the model to the ice-ice friction coefficient

728 Concerning contact forces, in a real iceberg-terminus contact, the processes involved  
729 might be complex given that the surfaces in contact are not flat, that water should act  
730 as a lubricant, and that the ice may break at some locations. Inversion of seismic records  
731 gives the forces applied by the iceberg to the terminus, with inclination angle  $\delta$  always  
732 smaller than  $30^\circ$  and usually below  $10^\circ$  [Tsai and Ekström, 2007]. This leads to vertical-  
733 to-horizontal force ratios  $F_z/F_x = \tan \delta$  lower than 0.58 and 0.18, respectively. If we  
734 assume that the vertical force component comes from frictional shear on the calving front  
735 only, the ice-ice global friction coefficient should generally satisfy  $\mu < 0.18$ . On the other  
736 hand, the value of ice-ice friction is highly variable depending on the sliding velocity and  
737 temperature [e.g. Schulson and Fortt, 2012]. Oksanen and Keinonen [1982] measured a  
738 small value of the kinetic friction  $\mu < 0.05$  for a range of velocities between 0.5 and 3 m.s<sup>-1</sup>  
739 and temperature close to the melting point ( $-2^\circ$  C), primarily due to friction-generated  
740 heat and local ice-melting. Our modeling results indicate that, for km-scale icebergs, the  
741 relative sliding velocity  $v_s$  is lower than 5 m.s<sup>-1</sup>. Oksanen and Keinonen [1982] further  
742 show that  $\mu$  increases as a function of  $v_s^{1/2}$ . However, the extrapolation of dry ice-ice  
743 experiment measurements to the field environment and glacier front conditions is clearly  
744 a difficult task and therefore  $\mu$  can be considered to be an unconstrained parameter  
745 within a range of small values. Here, for the sake of simplicity, we use a constant friction  
746 coefficient. We ran several computations under the conditions given in section 2. Testing  
747 the effect of  $\mu$  values in the range 0-0.1, we find that a 0.05 increase of  $\mu$  leads to a small  
748 decrease of the force amplitude and a negligible rise of its duration, the change of both  
749 being less than 1%. We therefore use  $\mu = 0$  in the following study (Table 1).

## References

- 750 Amundson, J., M. Truffer, M. Lüthi, M. Fahnestock, M. West, and R. Motyka (2008),  
751 Glacier, fjord, and seismic response to recent large calving events, jakobshavn isbræ,  
752 greenland, *Geophysical Research Letters*, *35*(L22501).
- 753 Amundson, J. M., M. Fahnestock, M. Truffer, J. Brown, M. P. Lüthi, and R. J. Motyka  
754 (2010), Ice mélange dynamics and implications for terminus stability, jakobshavn isbræ,  
755 greenland, *Journal of Geophysical Research: Earth Surface (2003–2012)*, *115*(F01005).
- 756 Amundson, J. M., J. C. Burton, and S. Correa-Legisos (2012a), Impact of hydrodynamics  
757 on seismic signals generated by iceberg collisions, *Annals of Glaciology*, *53*(60), 106–112.
- 758 Amundson, J. M., J. F. Clinton, M. Fahnestock, M. Truffer, M. P. Lüthi, and R. J. Motyka  
759 (2012b), Observing calving-generated ocean waves with coastal broadband seismome-  
760 ters, jakobshavn isbræ, greenland, *Annals of Glaciology*, *53*(60), 79–84.
- 761 Bamber, J. L., R. L. Layberry, and S. Gogineni (2001), A new ice thickness and bed data  
762 set for the greenland ice sheet: 1. measurement, data reduction, and errors, *Journal of*  
763 *Geophysical Research: Atmospheres*, *106*(D24), 33,773–33,780.
- 764 Besson, J., and R. Foerch (1997), Large scale object-oriented finite element code design,  
765 *Computer Methods in Applied Mechanics and Engineering*, *142*(1), 165–187.
- 766 Brennen, C. (1982), A review of added mass and fluid inertial forces, *NASA STI/Recon*  
767 *Technical Report N, 82*.
- 768 Burton, J., J. Amundson, D. Abbot, A. Boghosian, L. M. Cathles, S. Correa-Legisos,  
769 K. Darnell, N. Guttenberg, D. Holland, and D. MacAyeal (2012), Laboratory investi-  
770 gations of iceberg capsize dynamics, energy dissipation and tsunamigenesis, *Journal of*  
771 *Geophysical Research: Earth Surface (2003–2012)*, *117*(F01007).

- 772 Castelnau, O., P. Duval, M. Montagnat, and R. Brenner (2008), Elastoviscoplastic mi-  
773 cromechanical modeling of the transient creep of ice, *Journal of Geophysical Research:*  
774 *Solid Earth*, 113(B11203).
- 775 De Juan, J., P. Elósegui, M. Nettles, T. B. Larsen, J. L. Davis, G. S. Hamilton, L. A.  
776 Stearns, M. L. Andersen, G. Ekström, A. P. Ahlstrøm, et al. (2010), Sudden increase  
777 in tidal response linked to calving and acceleration at a large greenland outlet glacier,  
778 *Geophysical Research Letters*, 37(L12501).
- 779 Ekström, G., and C. P. Stark (2013), Simple scaling of catastrophic landslide dynamics,  
780 *Science*, 339(6126), 1416–1419.
- 781 Ekström, G., M. Nettles, and G. A. Abers (2003), Glacial earthquakes, *Science*, 302(5645),  
782 622–624.
- 783 Favreau, P., A. Mangeney, A. Lucas, G. Crosta, and F. Bouchut (2010), Numerical mod-  
784 eling of landquakes, *Geophysical Research Letters*, 37(15).
- 785 Francavilla, A., and O. Zienkiewicz (1975), A note on numerical computation of elastic  
786 contact problems, *International Journal for Numerical Methods in Engineering*, 9(4),  
787 913–924.
- 788 Hilber, H. M., T. J. Hughes, and R. L. Taylor (1977), Improved numerical dissipation for  
789 time integration algorithms in structural dynamics, *Earthquake Engineering & Struc-*  
790 *tural Dynamics*, 5(3), 283–292.
- 791 Howat, I. M., I. Joughin, and T. A. Scambos (2007), Rapid changes in ice discharge from  
792 greenland outlet glaciers, *Science*, 315(5818), 1559–1561.
- 793 James, T. D., T. Murray, N. Selmes, K. Scharrer, and M. OLeary (2014), Buoyant flexure  
794 and basal crevassing in dynamic mass loss at helheim glacier, *Nature Geoscience*, 7(8),

795 593–596.

796 Jean, M. (1995), Frictional contact in collections of rigid or deformable bodies: numerical  
797 simulation of geomaterial motions, *Studies in Applied Mechanics*, 42, 463–486.

798 Joughin, I., W. Abdalati, and M. Fahnestock (2004), Large fluctuations in speed on  
799 greenland’s jakobshavn isbrae glacier, *Nature*, 432(7017), 608–610.

800 Krug, J. W. O. G., J., and G. Durand (2014), Combining damage and fracture mechanics  
801 to model calving, *The Cryosphere*, 8, 2101–2117.

802 Mac Cathles, L., L. Kaluziński, and J. Burton (2015), Laboratory investigations of seis-  
803 micity caused by iceberg calving and capsize, in *AGU Fall Meeting Abstracts*.

804 MacAyeal, D. R., T. A. Scambos, C. L. Hulbe, and M. A. Fahnestock (2003), Catastrophic  
805 ice-shelf break-up by an ice-shelf-fragment-capsize mechanism, *Journal of Glaciology*,  
806 49(164), 22–36.

807 Montagnat, M., O. Castelnau, P. Bons, S. Faria, O. Gagliardini, F. Gillet-Chaulet,  
808 F. Grennerat, A. Griera, R. A. Lebensohn, H. Moulinec, et al. (2014), Multiscale mod-  
809 eling of ice deformation behavior, *Journal of Structural Geology*, 61, 78–108.

810 Moretti, L., A. Mangeney, Y. Capdeville, E. Stutzmann, C. Huggel, D. Schneider, and  
811 F. Bouchut (2012), Numerical modeling of the mount steller landslide flow history and  
812 of the generated long period seismic waves, *Geophysical Research Letters*, 39(L16402).

813 Moretti, L., K. Allstadt, A. Mangeney, Y. Capdeville, E. Stutzmann, and F. Bouchut  
814 (2015), Numerical modeling of the mount meager landslide constrained by its force  
815 history derived from seismic data, *Journal of Geophysical Research: Solid Earth*, 120(4),  
816 2579–2599.

- 817 Munson, B. R., A. P. Rothmayer, T. H. Okiishi, and W. W. Huebsch (2012), *Fundamentals*  
818 *of fluid mechanics*, John Wiley & Sons.
- 819 Murray, T., M. Nettles, and N. Selmes (2015a), Reverse glacier motion during iceberg  
820 calving and the cause of glacial earthquakes, *Science*, *349*(6245), 305–308.
- 821 Murray, T., N. Selmes, T. D. James, S. Edwards, I. Martin, T. O’Farrell, R. Aspey, I. Rutt,  
822 M. Nettles, and T. Baugé (2015b), Dynamics of glacier calving at the ungrounded  
823 margin of helheim glacier, southeast greenland, *Journal of Geophysical Research: Earth*  
824 *Surface*, *120*(6), 964–982.
- 825 Nettles, M., and G. Ekström (2010), Glacial earthquakes in greenland and antarctica,  
826 *Annual Review of Earth and Planetary Sciences*, *38*, 467–491.
- 827 Oksanen, P., and J. Keinonen (1982), The mechanism of friction of ice, *Wear*, *78*(3),  
828 315–324.
- 829 Olsen, K. G., and M. Nettles (2017), Patterns in glacial-earthquake activity around green-  
830 land, 2011–13, *Journal of Glaciology*, *63*(242), 1077–1089.
- 831 O’Neel, S., H. Marshall, D. McNamara, and W. Pfeffer (2007), Seismic detection and  
832 analysis of icequakes at columbia glacier, alaska, *Journal of Geophysical Research: Earth*  
833 *Surface (2003–2012)*, *112*(F03S23).
- 834 Petrenko, V., and R. Whitworth (1999), *Physics of ice*, 373 pp.
- 835 Podolskiy, E. A., and F. Walter (), Cryoseismology, *Reviews of Geophysics*, *54*(4), 708–  
836 758, doi:10.1002/2016RG000526.
- 837 Rosenau, R., E. Schwalbe, H.-G. Maas, M. Baessler, and R. Dietrich (2013), Grounding  
838 line migration and high-resolution calving dynamics of jakobshavn isbræ, west green-  
839 land, *Journal of Geophysical Research: Earth Surface*, *118*(2), 382–395.

- 840 Schulson, E. M., and A. L. Fortt (2012), Friction of ice on ice, *Journal of Geophysical*  
841 *Research: Solid Earth*, 117(B12).
- 842 Sergeant, A., A. Mangeney, E. Stutzmann, J.-P. Montagner, F. Walter, L. Moretti, and  
843 O. Castelnau (2016), Complex force history of a calving-generated glacial earthquake  
844 derived from broadband seismic inversion, *Geophysical Research Letters*, 43(3), 1055–  
845 1065.
- 846 Smith, S. D., and E. G. Banke (1983), The influence of winds, currents and towing forces  
847 on the drift of icebergs, *Cold Regions Science and Technology*, 6(3), 241–255.
- 848 Tsai, V. C., and G. Ekström (2007), Analysis of glacial earthquakes, *Journal of Geophys-*  
849 *ical Research: Earth Surface (2003–2012)*, 112(F03S22).
- 850 Tsai, V. C., J. R. Rice, and M. Fahnestock (2008), Possible mechanisms for glacial earth-  
851 quakes, *Journal of Geophysical Research: Earth Surface (2003–2012)*, 113(F03014).
- 852 Vaughan, D. G. (1995), Tidal flexure at ice shelf margins, *Journal of Geophysical Research:*  
853 *Solid Earth*, 100(B4), 6213–6224.
- 854 Veitch, S. A., and M. Nettles (2012), Spatial and temporal variations in greenland glacial-  
855 earthquake activity, 1993–2010, *Journal of Geophysical Research: Earth Surface (2003–*  
856 *2012)*, 117(F002412).
- 857 Wagner, T. J., T. D. James, T. Murray, and D. Vella (2016), On the role of buoyant  
858 flexure in glacier calving, *Geophysical Research Letters*, 43(1), 232–240A.
- 859 Walter, F., S. O’Neel, D. McNamara, W. Pfeffer, J. N. Bassis, and H. A. Fricker (2010),  
860 Iceberg calving during transition from grounded to floating ice: Columbia glacier, alaska,  
861 *Geophysical Research Letters*, 37(15).

- 862 Walter, F., J. M. Amundson, S. O’Neel, M. Truffer, M. Fahnestock, and H. A. Fricker  
863 (2012), Analysis of low-frequency seismic signals generated during a multiple-iceberg  
864 calving event at jakobshavn isbræ, greenland, *Journal of Geophysical Research: Earth  
865 Surface (2003–2012)*, 117(F1).
- 866 Walter, F., M. Olivieri, and J. F. Clinton (2013), Calving event detection by observation  
867 of seiche effects on the greenland fjords, *Journal of Glaciology*, 59(213), 162–178.
- 868 Wendel, K. (1956), Hydrodynamic masses and hydrodynamic moments of inertia, Ph.D.  
869 thesis, Hamburg, translated to English by E.N. Labouvie and Avis Borden, and available  
870 at <https://dome.mit.edu/handle/1721.3/51294>.
- 871 Xie, S., T. H. Dixon, D. Voytenko, D. M. Holland, D. Holland, and T. Zheng (2016),  
872 Precursor motion to iceberg calving at jakobshavn isbræ, greenland, observed with  
873 terrestrial radar interferometry, *Journal of Glaciology*, 62(236), 1134–1142.
- 874 Yamada, M., A. Mangeney, Y. Matsushi, and L. Moretti (2018a), Estimation of dynamic  
875 friction process of the akatani landslide based on the waveform inversion and numerical  
876 simulation, *Geophysical Journal International*, 206, 1479–1486.
- 877 Yamada, M., A. Mangeney, Y. Matsushi, and T. Matsuzawai (2018b), Estimation of  
878 dynamic friction and movement history of large landslides, *Landslides*, (F1), doi:10.  
879 1007/s10346-018-1002-4.
- 880 Yvin, C., A. Leroyer, M. Visonneau, and P. Queutey (2018), Added mass evaluation with  
881 a finite-volume solver for applications in fluid–structure interaction problems solved  
882 with co-simulation, *Journal of Fluids and Structures*, 81, 528–546.
- 883 Zhao, J., L. Moretti, A. Mangeney, E. Stutzmann, H. Kanamori, Y. Capdeville, E. Calder,  
884 C. Hibert, P. Smith, P. Cole, and A. LeFriant (2014), Model space exploration for

885 determining landslide source history from long-period seismic data, *Pure and Applied*  
886 *Geophysics*, pp. 1–25, doi:10.1007/s00024-014-0852-5.

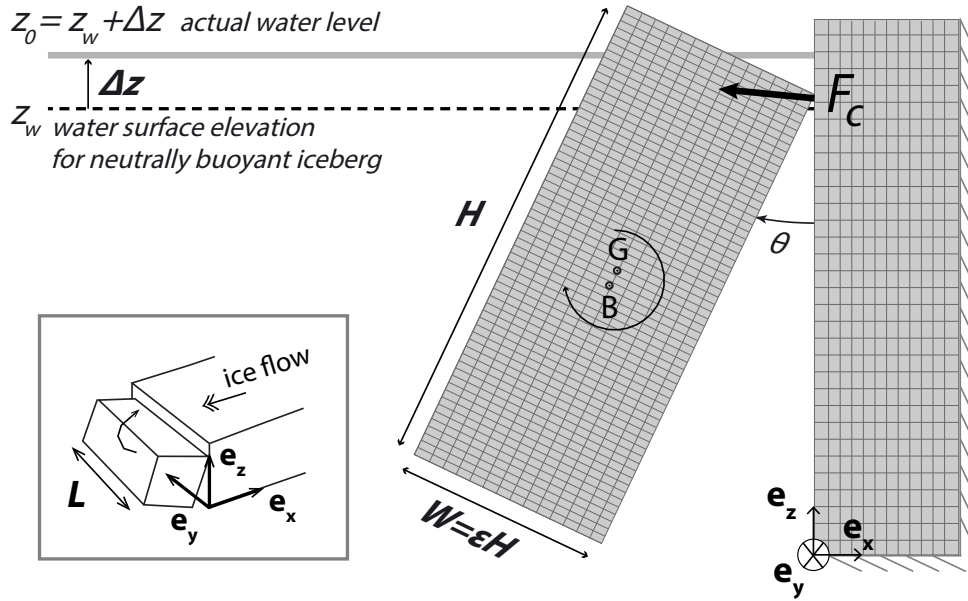


**Figure 1.** Geometry and parameters of the system: iceberg aspect ratio  $\epsilon$ , height  $H$  and perturbation of the water level  $\Delta z$  for initial hydrostatic equilibrium of the ice-block. The iceberg across-glacier length  $L$  is in the  $y$ -direction.  $G$  and  $B$  are the center of mass of the iceberg and of its submerged part, respectively. The ice wall is fixed vertically and horizontally. The contact force  $F_c$  is integrated over the vertical rear face of the wall.

**Table 1.** List of model parameters used in all simulations.

Parameter	Symbol	Value(s)
Iceberg height	$H$	500-1050 m
Iceberg aspect ratio	$\epsilon$	0.1-0.7
Iceberg length	$L$	500-5000 m
Ice Young's modulus	$E$	9.3 GPa
Ice Poisson coefficient	$\nu$	0.3
Ice-ice friction	$\mu$	0
Ice density	$\rho_i$	917 kg.m <sup>-3</sup>
Sea water density	$\rho_w$	1025 kg.m <sup>-3</sup>

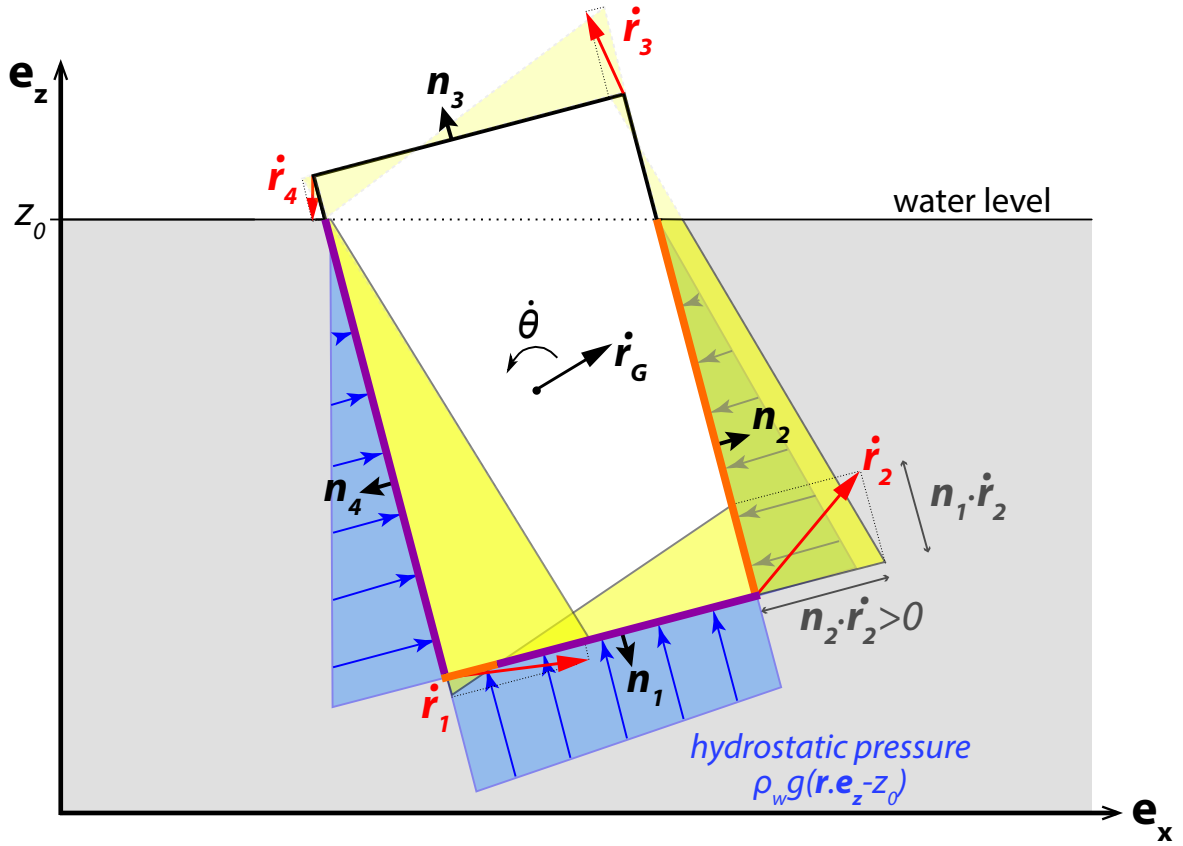


**Figure 2.** Illustration of a 2D icebergs capsizing in water and pressures applied on the surface elements. Here is represented a box-shaped icebergs with surface elements equal to the side length, with local outward normal vector  $\mathbf{n}(\mathbf{r})$ . The static water pressure (inward blue arrows) applied to the icebergs boundary increases linearly with surface element depth. The yellow areas represent the profiles of normal velocities  $v_n(\mathbf{r}) = \dot{\mathbf{r}} \cdot \mathbf{n}$  along each boundary segment. Submerged surface boundaries are plotted in purple when the pressure related to drag (equation 2) is collinear to the local normal vector  $\mathbf{n}$  (toward the outside of the icebergs) as the local normal component of the velocity is negative ( $\dot{\mathbf{r}} \cdot \mathbf{n} < 0$ ). On the opposite, orange boundaries are when the pressure drag direction is toward the inside of the icebergs as  $\dot{\mathbf{r}} \cdot \mathbf{n} > 0$ .

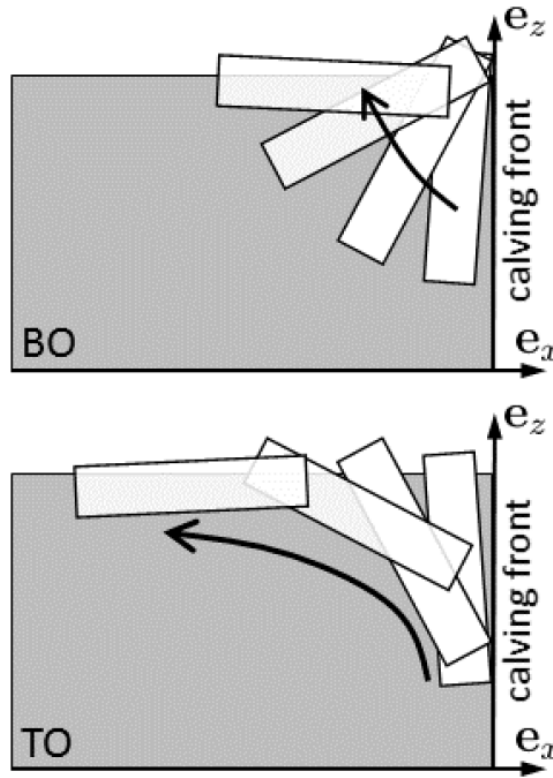


**Figure 3.** For BO calving events, hydrodynamic forces push the upper right iceberg tip against the calving front. For TO events, they make the iceberg move naturally away from the calving front.

**Table 2.** Force amplitudes and timescale responses to tipping iceberg parameters.

Quantity	Notation	Unit	Bottom-out	Top-out
Force linear density	$F_c$	N/m	$7 \times 10^6 - 6.9 \times 10^7$	$8.2 \times 10^6 - 7.3 \times 10^7$
Total force	$LF_c$	N	$3 \times 10^9 - 3.5 \times 10^{11}$	$4.1 \times 10^9 - 3.7 \times 10^{11}$
Force magnitude <sup>1</sup>	$A$	kg.m	$3 \times 10^{12} - 9.9 \times 10^{14}$	$5.7 \times 10^{12} - 8.2 \times 10^{14}$
CSF magnitude <sup>2</sup>	$A_{CSF}$	kg.m	$6 \times 10^{11} - 1.4 \times 10^{14}$	$5.6 \times 10^{11} - 2 \times 10^{14}$
Duration of the force	$T$	s	100-300	100-250

<sup>1</sup> From the double-integration in time of  $F_c(t)$ .

<sup>2</sup> From the double-integration in time of CSF models that best fit  $F_c(t)$  when filtered in the seismic band.

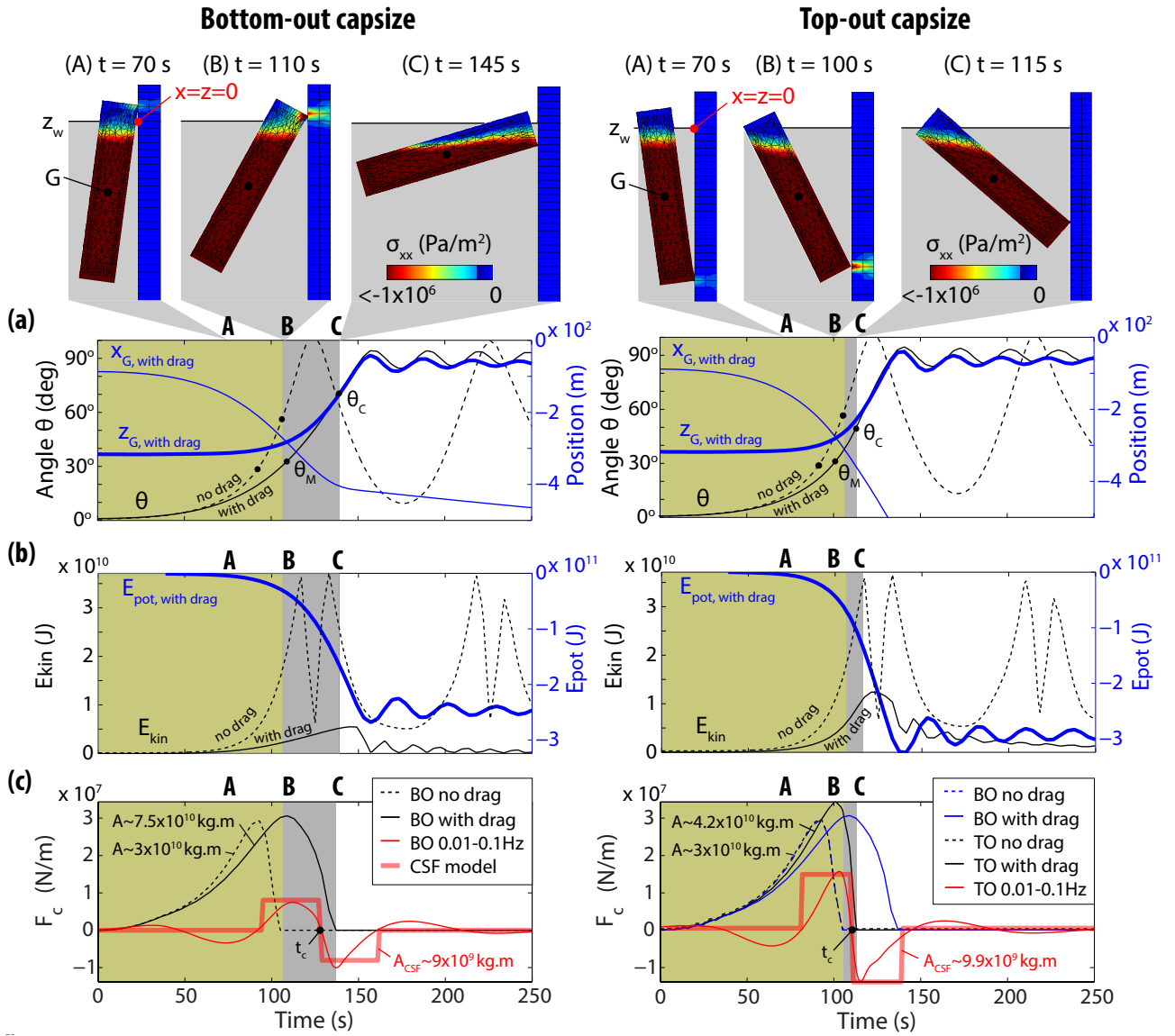


**Figure 4.** Results of bottom-out (left) and top-out (right) capsize simulations for an iceberg with  $\epsilon = 0.2$  and  $H = 800$  m. Top images illustrate capsize motions at different time steps: (A) when the iceberg is accelerating, (B) when the contact force with the wall is maximum and (C) at the loss of the iceberg-wall contact. The color scale represents the stress component  $\sigma_{xx}$  and is saturated beyond  $-1 \times 10^6$  Pa, to simplify the illustration. Variations with time of (a) angle of rotation ( $\theta$ , black curve) and coordinates  $x_G$  and  $z_G$  of the center of mass  $G$  (blue), (b) iceberg kinetic ( $E_{\text{kin}}$ , black) and potential ( $E_{\text{pot}}$ , blue) energies, (c) horizontal force density ( $F_c$ , black) and corresponding 0.01-0.1 Hz bandpass filtered force (red). The thick red curve shows the CSF model that best fits the force in the seismic band. In each graph, dashed curves represent time-series of  $\theta$ ,  $E_{\text{kin}}$  and  $F_c$  when water drag is not accounted for. Gray-shaded boxes indicate the time range when the iceberg is in contact with the wall (i.e.  $F_c > 0$  N and  $\theta \leq \theta_C$ ). Same for yellow boxes but for capsize simulations without drag.  $\theta_M$  and  $\theta_C$  in (a) indicate the angles for maximum contact force and loss of iceberg/wall contact, respectively.

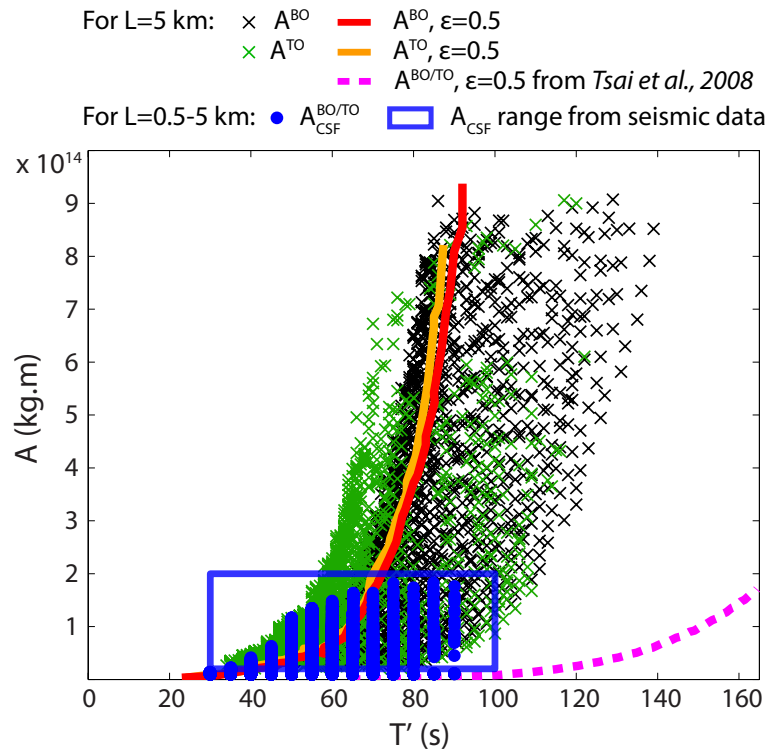


**Figure 5.** Force magnitudes  $A$  (kg.m) versus durations  $T'$  which corresponds to the effective duration of the force. Crosses are for BO (black) and TO (green) capsizes with iceberg height  $H = 100 - 1000$  m, aspect ratio  $\epsilon = 0.1 - 0.7$  and length  $L = 5000$  m. Red and orange curves are for the specific value  $\epsilon = 0.5$ , for BO and TO respectively. The pink dashed curve indicates the results of *Tsai et al.* [2008] for the same iceberg dimensions, BO and TO together. Blue points are CSF magnitudes  $A_{CSF}$  computed by integrating twice the CSF models that fit the 0.01-0.1 Hz filtered forces generated by BO and TO capsizes of icebergs with lengths varying between 500 m and 5000 m. Computed  $A_{CSF}$  values are in the range of seismic observations (blue box) derived from glacial earthquake CSF inversions [*Tsai and Ekström, 2007; Veitch and Nettles, 2012*].

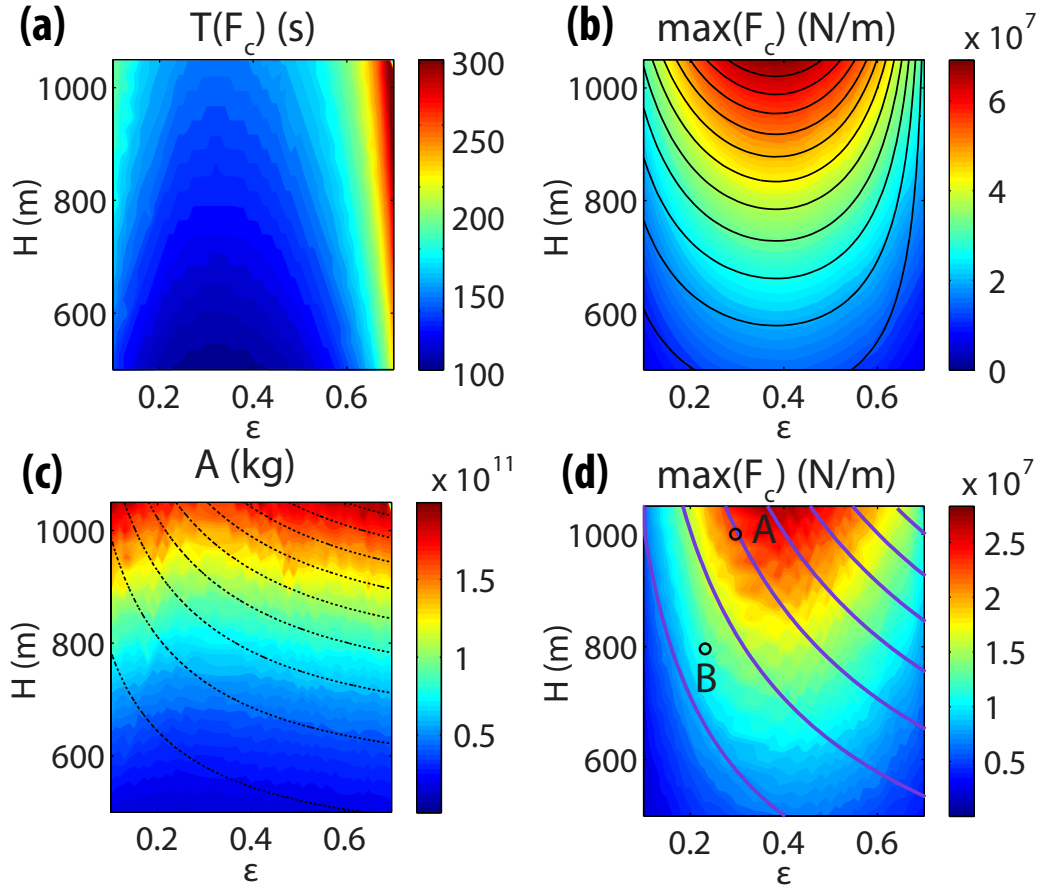


**Figure 6.** Variations of the BO contact force (a) duration  $T$ , (b) maximum amplitude and (c) magnitude  $A$  with iceberg dimensions  $H$  and  $\epsilon$ . Results are for the force linear density, which is equivalent to the forces of icebergs with  $L = 1$  m. (d) shows the force amplitude variations when filtered in the seismic band 0.01-0.1 Hz. Contour black curves on (b) show the analytical function  $H^{2.6}\epsilon(\sqrt{1-\epsilon^2}-\epsilon)$  for the maximum amplitude of  $F_c$ . Contour black curves on (c) show the analytical function of the contact force magnitude  $A \propto H^3\epsilon(\sqrt{1+\epsilon^2}-\epsilon)$  when hydrodynamic effects are not accounted for [Tsai *et al.*, 2008; Amundson *et al.*, 2012a]. The purple contours on (d) show lines along which the iceberg volume  $\epsilon H^2 L$  is constant. Black circles A and B indicate the iceberg dimensions and force magnitudes or amplitudes derived from seismic inversions of two glacial earthquakes (see text for details).

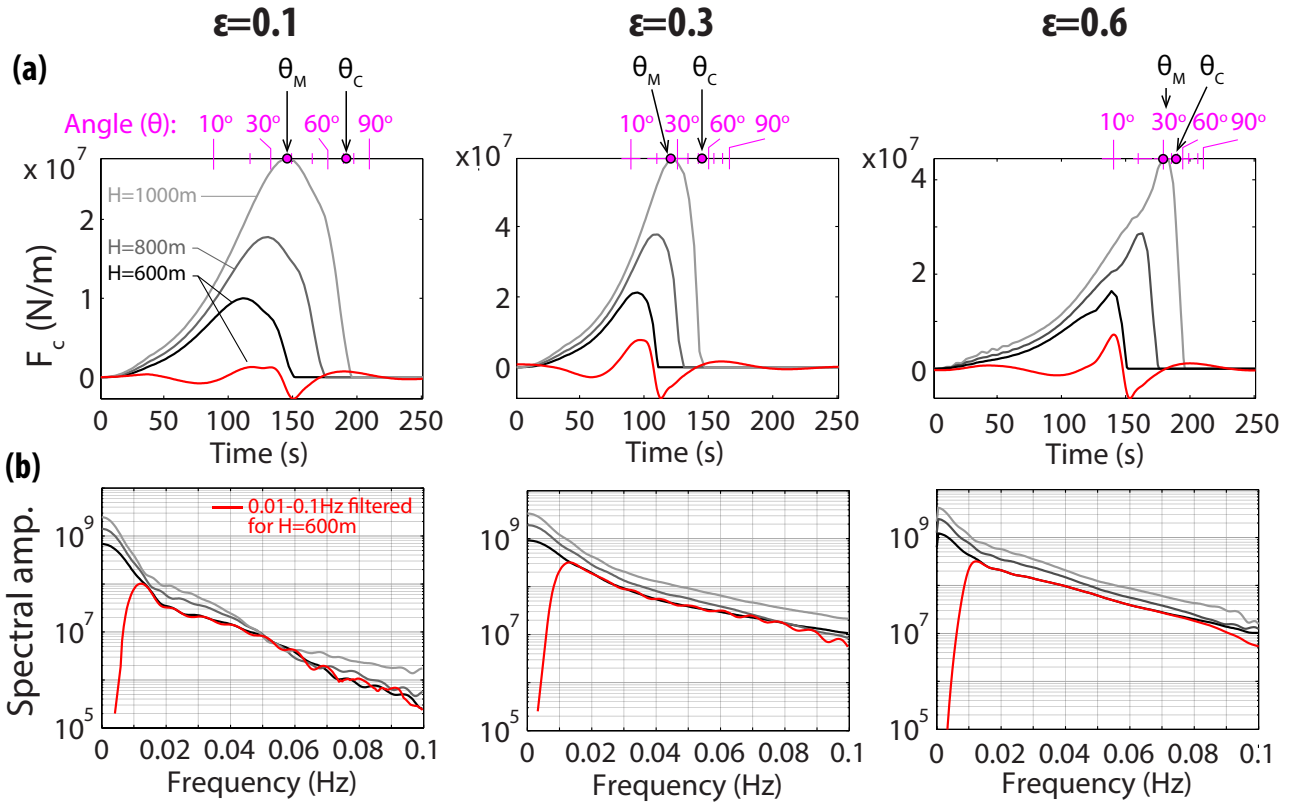


**Figure 7.** (a) Variations of the force history for three BO iceberg heights  $H = 600$  m, 800 m and 1000 m, and aspect ratios  $\epsilon = 0.1, 0.3$  and  $0.6$ . The red curves show the 0.01-0.1 Hz filtered forces for  $H = 600$  m. The rotation angle  $\theta$  for 1000 m high iceberg capsizes are indicated in purple at the top of each panel. (b) Variations of spectral amplitudes with frequency, associated with each modeled force.

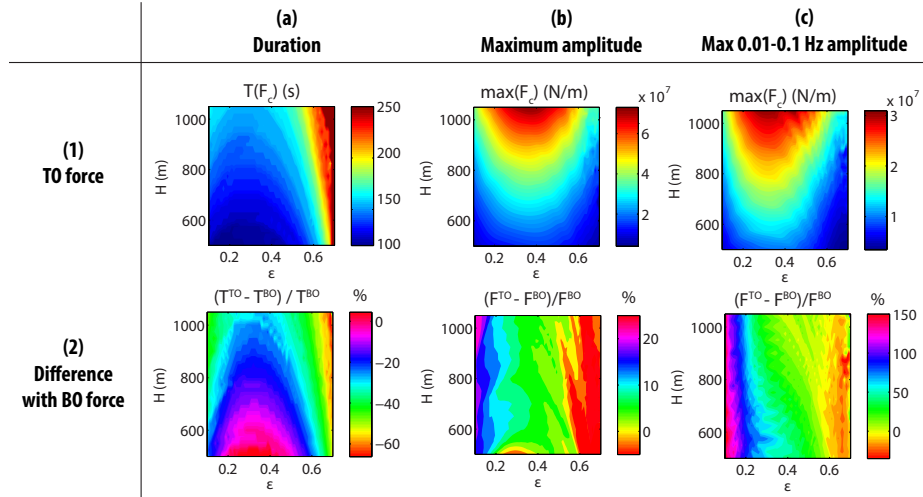


**Figure 8.** Top panels (1): Variations of the (a) duration  $T$  and (b-c) maximum amplitude of the force with  $\epsilon$  and  $H$ , for TO events, when  $L = 1$  m. Bottom panels (2): Same as in (1) but for the differences between TO and BO features, i.e.  $(F_c^{TO} - F_c^{BO}) / F_c^{BO}$ . Represented values are in %. Positive (vs. negative) values indicate larger (vs. smaller) TO force amplitudes or durations, with respect to BO.

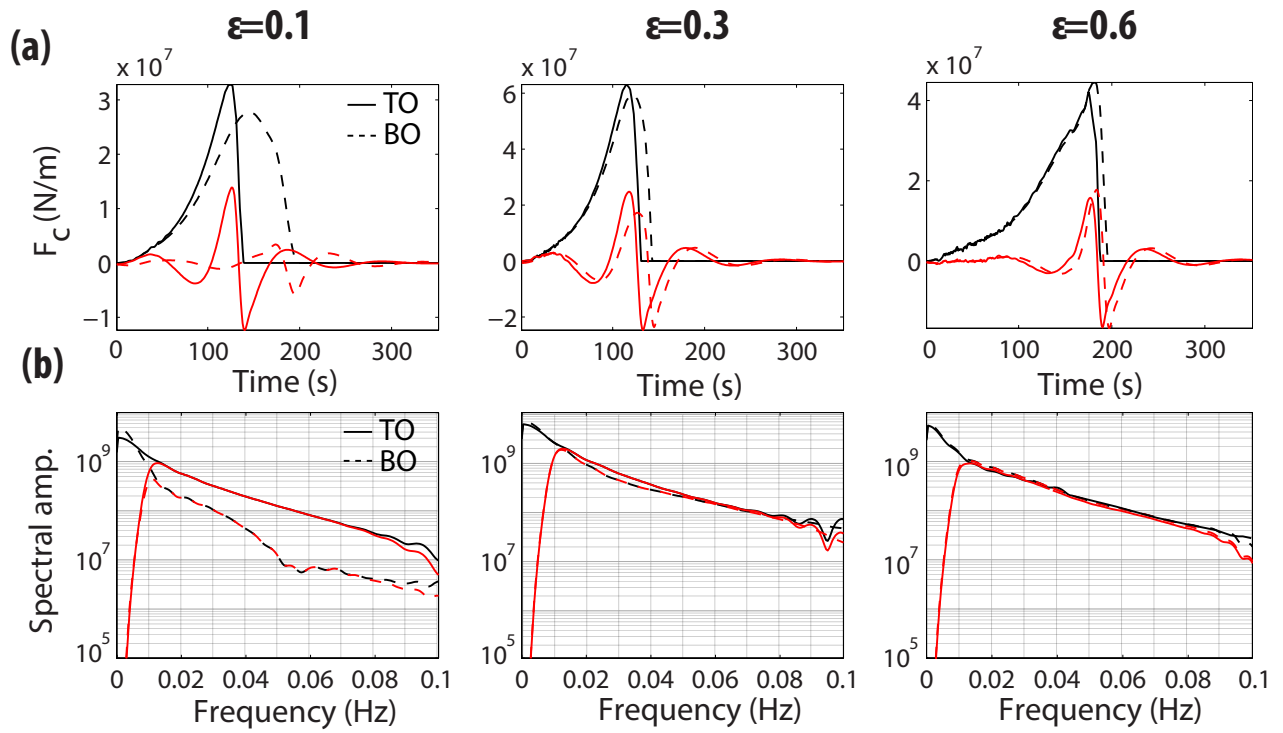


**Figure 9.** (a) Variations of the force history for TO (solid curves) and BO (dashed curves) iceberg capsizes with  $\epsilon = 0.1, 0.3$  and  $0.6$  and  $H = 1000$  m. The red curves show the 0.01-0.1 Hz filtered forces. (b) Variations of spectral amplitudes with frequency, associated with each force model.

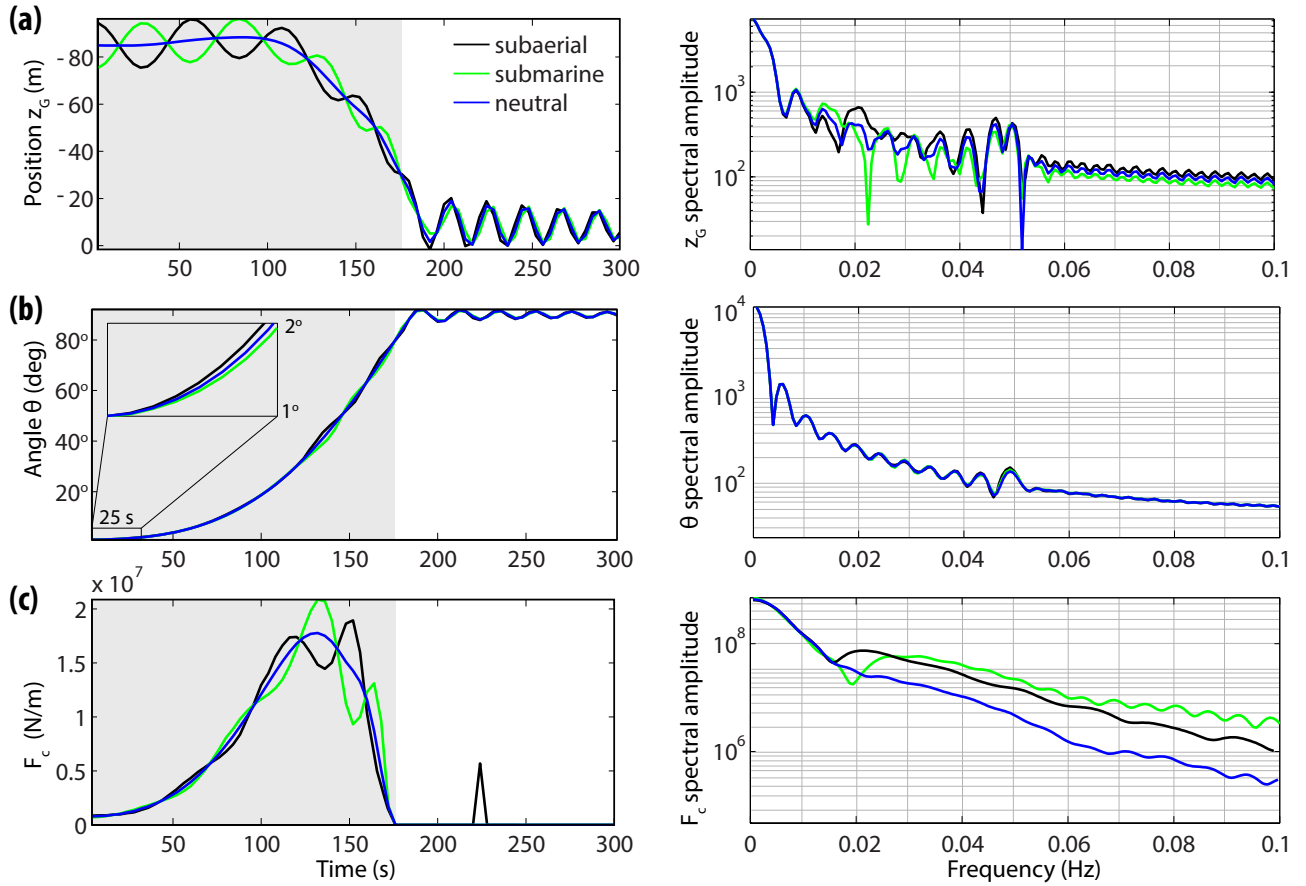


**Figure 10.** Time-series of the (a) vertical positions  $z_G(t)$ , (b) angle  $\theta(t)$ , (c) horizontal force  $F_c(t)$  and associated spectral energy distribution for submarine (green), subaerial (black) and initially neutrally buoyant (blue) capsizing icebergs. Results are for BO icebergs with  $\epsilon = 0.1$ ,  $H = 800$  m and  $|\Delta z| = 10$  m.

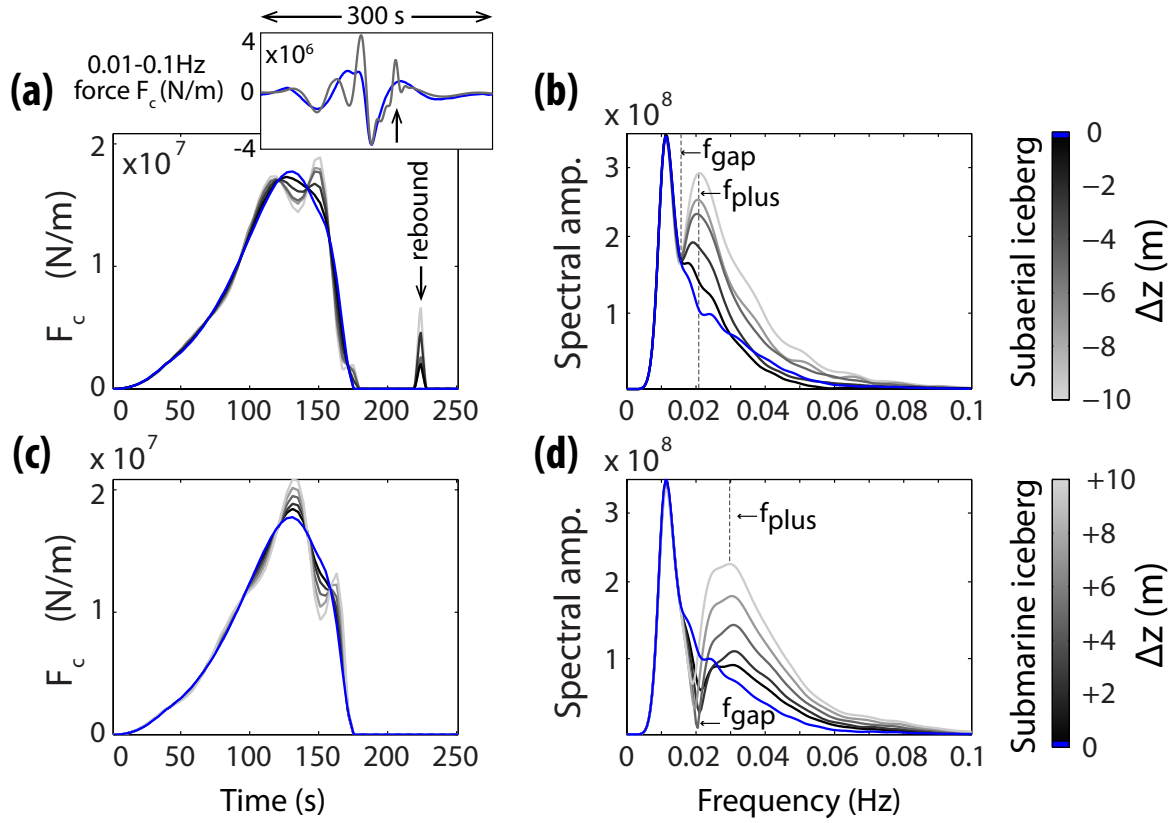


**Figure 11.** Effects of initial conditions for the hydrostatic equilibrium of the capsizing iceberg on the force (a and c) history and (b and d) spectral amplitudes. For more visibility, spectral amplitudes are for the 0.01-0.1 Hz filtered time-series. The blue curves are results for neutrally buoyant icebergs (i.e.  $\Delta z = 0$  m). The different shades of gray curves are results for different non-zero  $|\Delta z|$  values. Top graphs (a-b) are for subaerial icebergs ( $\Delta z < 0$ ). Bottom graphs (c-d) are for submarine icebergs ( $\Delta z > 0$ ). Results are shown here for BO icebergs with  $\epsilon = 0.1$ ,  $H = 800$  m. The inset box above the top-left panel represents the forces filtered in the seismic band 0.01-0.1 Hz associated with the capsizes of a neutral iceberg (blue curve) and a subaerial iceberg (gray curve). The black arrow indicates the seismic signature for the iceberg impact on the terminus, once it has fully capsized.

**Figure 12.** Comparison of the forces (a) simulated with iceberg capsize models and (b) inverted from seismic data, both filtered between 0.01-0.1 Hz, as well as the associated normalized spectrograms and power spectra. These simulated and inverted forces are for systems out of buoyant equilibrium (i. e.  $\Delta z \neq 0$ ). For field data in Greenland (column (b)), locations of the calving events and GLISN stations used in the waveform inversion are indicated on inset maps by red stars and yellow triangles, respectively. The power spectra panels show the forces inverted from seismic data (red curves), modeled with either submarine or subaerial icebergs (black curves), and modeled with neutral icebergs (blue curves). The comparison between models and data show that seismic data spectral peaks or gaps indicated by arrows can be explained by the initial buoyant state of the capsizing icebergs, especially when they are out of their flotation level when they start calving.

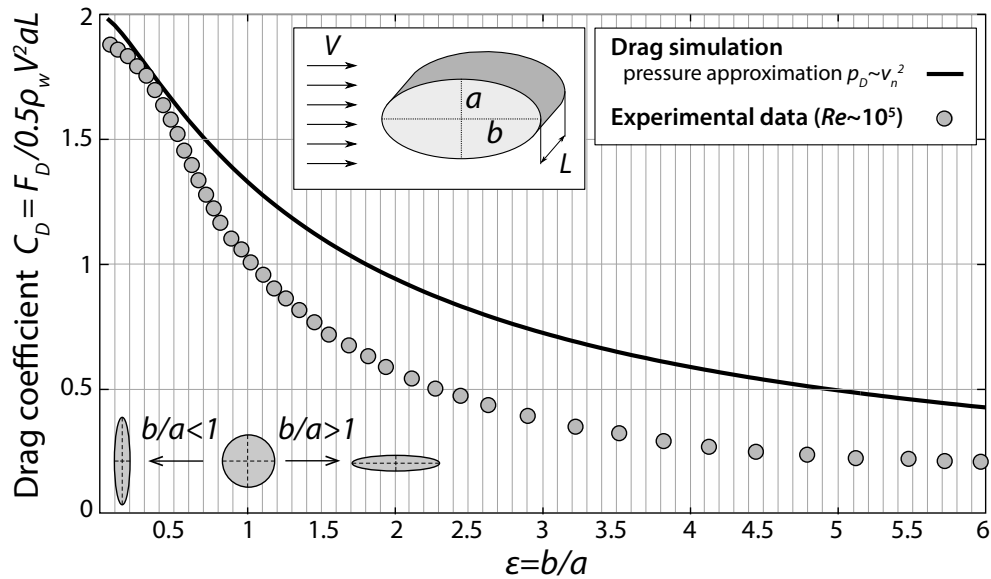


**Figure A1.** Drag coefficients  $C_D$  computed with the pressure drag approximation from equation 3 (solid curve) and experimental measurements (circles) from *Munson et al.* [2012]. Results are for ellipses of various aspect ratios  $b/a$  (semi-axes  $a$  and  $b$ ) moving in water with relative velocity  $V$  at  $Re \sim 10^5$ .